

## REVIEW

[View Article Online](#)  
[View Journal](#) | [View Issue](#)



Cite this: *Chem. Sci.*, 2021, **12**, 6238

## On the underestimated influence of synthetic conditions in solid ionic conductors

Ananya Banik,<sup>a</sup> Theodosios Famprakis,<sup>bd</sup> Michael Ghidiu,<sup>c</sup> Saneyuki Ohno,<sup>bd</sup> Marvin A. Kraft<sup>a</sup> and Wolfgang G. Zeier<sup>bd</sup>                        <img alt="ORCID iD icon" data-bbox="2

## 1. Introduction

Since their commercial introduction,<sup>1,2</sup> rechargeable lithium-ion batteries have become necessary parts of our daily lives, especially in the realms of transportation and mobile electronics. In these areas, demands for smaller, safer, and more energy-dense batteries are only expected to increase in the coming years.<sup>3</sup> By far the most used architecture to date involves solid electrodes and a liquid electrolyte (generally a lithium salt dissolved in organic solvents).<sup>2</sup> Problems with the liquid electrolyte systems involve flammability (in the case of cell short-circuits or rupture),<sup>4</sup> lowered transference numbers,<sup>5,6</sup> and prevalence of dendrite growth leading to shorting, disallowing use of higher-energy-density lithium metal anodes.<sup>7</sup> Though dendrite formation and cell short-circuiting is intrinsic to the use of lithium metal electrode irrespective of the nature of an electrolyte,<sup>8</sup> the ease of growth of dendrites is especially a problem for liquid electrolyte cell when combined with flammability concerns. Engineering solutions have been proposed for these issues,<sup>7</sup> but a more promising path altogether is the use of solid electrolytes.<sup>9</sup> Due to understandably poorer conduction, many solids were not initially thought of as

viable, with some focus on polymers or supported gels.<sup>7</sup> However, the emergence of superionic solids that could conduct lithium and sodium nearly as well as some liquids brought extreme interest to the concept of the all-solid-state battery.<sup>10-12</sup> These materials offer excellent ionic conductivities,<sup>11,13-15</sup> low electronic conductivity saving the cell from self-discharge,<sup>16</sup> a transference number near unity which further can boost the power density of the cells.<sup>11</sup>

Typical solid ionic conductors include polymeric materials;<sup>17</sup> oxides such as LISICON (lithium superionic conductor)<sup>18,19</sup> and NASICON (sodium superionic conductor and Li-ion conducting sodium superionic conductor)<sup>20</sup> – type phosphates and garnets such as  $\text{Li}_7\text{La}_3\text{Zr}_2\text{O}_{12}$  (LLZO);<sup>21</sup> sulfides such as thio-LISICONs<sup>22</sup> and thiophosphates, including the argyrodites  $\text{Li}_6\text{PS}_5\text{X}$  (X = Cl, Br, I),<sup>13,14,23</sup>  $\text{Li}_{10}\text{MP}_2\text{S}_{12}$  (LMPS) (M = Si, Ge, Sn)<sup>11,15,24,25</sup> or  $\text{Na}_3\text{MS}_4$  (M = P, Sb)<sup>26,27</sup> and its substituted analogues.<sup>12</sup> Other materials such as the ternary halides, lithium hydride, and lithium nitride also garner interest.<sup>28-30</sup> All these materials have been reviewed in-depth in the literature so we suffice it to say here that each class spans a wide range of advantages and disadvantages in various properties: ionic and electronic conductivity, electrochemical stability windows, mechanical softness or brittleness,



*Michael Ghidiu earned his PhD in Materials science and Engineering in 2018 from Drexel University in Philadelphia characterizing novel 2D materials for energy storage (MXenes), and subsequently moved to Germany for post-doctoral work with Prof. Wolfgang Zeier, focusing on electrolyte development for solid-state batteries.*



*Marvin Kraft received his M.Sc. in Material Sciences from the Justus Liebig-University in Gießen. Currently, he is working in the group of Prof. Wolfgang Zeier as doctoral student, focusing his research onto the structure–transport relationship in sulfidic solid electrolytes.*



*Saneyuki Ohno received his PhD in Materials Science from California Institute of Technology in 2017. Following the post-doctoral research with Prof. Jürgen Janek and Prof. Wolfgang Zeier in the Institute of Physical Chemistry at Justus Liebig University Gießen with Humboldt research fellowship, he joined the Department of Applied Chemistry at Kyushu University as an Assistant Professor in 2020. His research interests include functional inorganic materials and composites with ion/electron/phonon transport for energy storage and conversion, e.g., solid electrolytes, thermoelectrics, and electrodes for solid-state batteries.*



*Wolfgang Zeier received his doctorate from the University of Mainz in 2013, followed by postdoctoral stays at the University of Southern California, the California Institute of Technology and Northwestern University. After leading an independent research group at the University of Giessen, he now holds a professorship for inorganic solid-state chemistry at the University of Muenster. His research interests are fundamental structure–property relationships in phonon and ionic transport as well as solid–solid interfaces in solid-state batteries.*



the energy required for synthesis and processing, cost of materials.<sup>30–32</sup> Ionic conductivity, however, retains a high focus as a key property for determining whether a candidate material will be acceptable for battery application.<sup>33,34</sup> Especially, considering the solid composite nature in absence of liquids, these solid-state batteries require fast ionic transport with ionic conductivities of cold-pressed materials ideally exceeding 10 mS cm<sup>−1</sup> in order to achieve high materials loading and high partial ionic conductivities.<sup>34,35</sup>

In this review we will focus on the inorganic ion conductors, which exhibit a large range of conductivities for similar or identical materials based on synthetic protocol. To illustrate how much of an effect is possible, Fig. 1 shows a graphical summary of a number of selected materials from the literature. The spread within a single class can be as much as five orders of magnitude, with differences arising from the ways the materials were made or treated; it is important to note, however, that these effects are attributable to the produced materials themselves and cannot be explained solely on the basis of differences in the conductivity measurement protocols.<sup>36</sup>

Tailoring structures to optimize ionic conductivity in solids is becoming better understood. Body-centred-cube-like structures with face-sharing tetrahedra are ideal to avail low ion-diffusion barrier and high conductivity.<sup>16,33</sup> Recent discoveries have reestablished the correlation between lattice dynamics and ionic transport.<sup>70–72</sup> The presence of soft, polarizable anionic

frameworks is responsible for widening of ion-diffusion pathway and low activation barrier.<sup>70</sup> However, because measurements on or implementation in batteries of solid electrolytes generally involve polycrystalline materials, a myriad of other phenomena can influence performance; these can be in turn very sensitive to the synthesis and treatment of the materials. Some of these phenomena include:

## Densification

Higher contact area and more percolation pathways not only lead to higher ion conductance but also allow complete electrochemical utilization of active materials.<sup>73</sup> Densification can result from *e.g.* sintering, or from pressure applied either prior to a measurement or during measurement.<sup>13,74,75</sup> For applied pressure, the elastic modulus, fracture toughness of the material are important. By use of softer materials, like the thiophosphates better connectivity with the adjacent phases like electrode materials can be achieved by allowing elastic-deformation as opposed to oxides; nevertheless, both the materials are prone to crack formation under stress due to low fracture toughness.<sup>70,73,76–78</sup>

## Particle morphology, orientation and grain size

Some materials are ionic conductors only in one or two dimensions.<sup>79</sup> Hence, changes in bulk conductivity can arise if there are differences in grain orientation, aspect ratio, or size.<sup>48,80</sup> Grain boundaries can also influence conductivity due to impurity segregation and, therefore, formation of space charge layer.

## Change in crystalline and amorphous content

Bulk materials with a fixed chemical composition often contain changing percentages of crystalline and amorphous regions.<sup>81</sup> These can have very different transport properties, with no general rule governing which has the higher conductivity. For instance, amorphous Li-thiophosphates are faster conductors than their crystalline counterparts, but for argyrodites, the crystalline phase has the higher conductivity.<sup>82–84</sup> Some phases, such as Li<sub>7</sub>P<sub>3</sub>S<sub>11</sub>, may always inherently exist as mixture of glassy and crystalline phases (or glass-ceramics).<sup>83,85</sup> This theme can also include local structural changes that are not reflected in the bulk crystal structure, as well as phase changes into different polymorphs, *e.g.* between  $\beta$  and  $\gamma$  forms of Li<sub>3</sub>PS<sub>4</sub>.<sup>86</sup>

## Change in local or bulk chemical composition

A bulk material of a given chemical composition can, under some circumstances, experience local changes in composition. Li<sub>7</sub>P<sub>3</sub>S<sub>11</sub>, for example, can undergo decomposition into the poor conductor Li<sub>4</sub>P<sub>2</sub>S<sub>6</sub> by reduction of P<sup>V</sup> to P<sup>IV</sup> with additional sulfur segregating to another phase.<sup>87</sup>

## Strain

Structures can, through various pathways, have strain that may lead to change in the lattice volume and thus differences in the

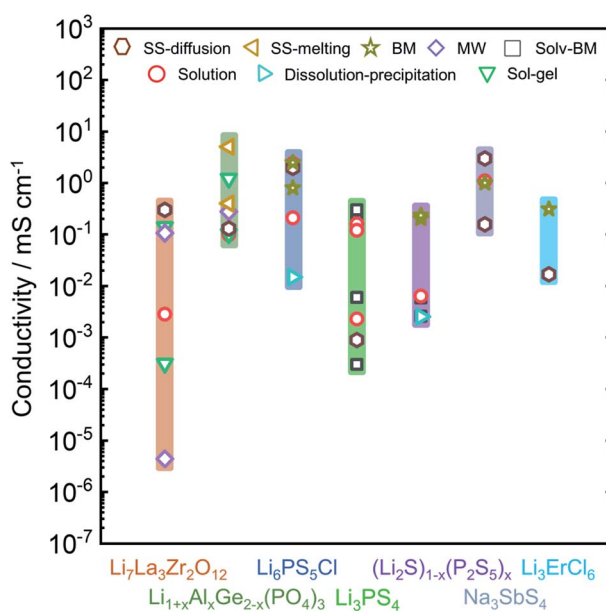


Fig. 1 Overview of the observed ionic conductivities for well-known Li-ion and Na-ion conducting electrolytes including Li<sub>7</sub>La<sub>3</sub>Zr<sub>2</sub>O<sub>12</sub>,<sup>37–43</sup> Li<sub>1+x</sub>Al<sub>x</sub>Ge<sub>2-x</sub>(PO<sub>4</sub>)<sub>3</sub>,<sup>44–51</sup> Li<sub>6</sub>PS<sub>5</sub>Cl,<sup>14,52–55</sup> Li<sub>3</sub>PS<sub>4</sub>,<sup>56–61</sup> (Li<sub>2</sub>S)<sub>x</sub>-(P<sub>2</sub>S<sub>5</sub>)<sub>100-x</sub>,<sup>62–65</sup> Na<sub>3</sub>SbS<sub>4</sub>,<sup>12,66–68</sup> and Li<sub>3</sub>ErCl<sub>6</sub> (ref. 69) as a function of synthetic condition. Conductivity can vary over orders of magnitude, based on the adopted synthesis route. Li<sub>1+x</sub>Al<sub>x</sub>Ge<sub>2-x</sub>(PO<sub>4</sub>)<sub>3</sub> column represents the conductivities for Li<sub>1+x</sub>Al<sub>x</sub>Ge<sub>2-x</sub>(PO<sub>4</sub>)<sub>3</sub> with x = 0.4, 0.5. (Li<sub>2</sub>S)<sub>x</sub>(P<sub>2</sub>S<sub>5</sub>)<sub>100-x</sub> column consists of conductivities data from non-crystalline phases of (Li<sub>2</sub>S)<sub>x</sub>(P<sub>2</sub>S<sub>5</sub>)<sub>100-x</sub> with x = 75, 80.



ability to conduct ions.<sup>81,88</sup> It is worth mentioning here that use of solid electrolytes in lithium ion battery does not solve the problem of lithium dendrite formation and cell short circuiting. Due to the lower density of the solid electrolyte, the presence of a porous network or internal cracking. Recent studies have predicted beneficial role of compressive force as an electrolyte processing parameter to prevent lithium penetration and dendritic degradation.<sup>89</sup>

### Structural disorder

A relatively new direction of exploration, some compositions contain atoms on different crystallographic sites that can be exchanged; a prime example is  $\text{Li}_6\text{PS}_5\text{Br}$  or the ternary lithium halides.<sup>69,84,90</sup> Disorder between the exchangeable sites can alter the activation barriers of ionic movement.

In this review, we wish to show how all these factors can be extremely important in determining the overall usefulness of a solid electrolyte material, and that synthesis and processing conditions can lead to such changes occurring, sometimes in combination. Understanding what will happen to a solid electrolyte throughout its production and how to control the processes is critical in producing optimized solid-state batteries.

## 2. Overview of possible synthetic conditions

In this section, common techniques of synthesis of ionic conductors will be reviewed in order to provide a baseline for the reader to follow the subsequent discussions of how synthesis parameters influence structures, chemistry, and transport. This will include high-temperature,

mechanochemical, solvent-based, and microwave techniques, with discussion on variable parameters such as precursor routes, temperature programming, mechanical energy input, and solvent selection. Table 1 summarizes the advantages and drawbacks of these synthesis techniques for solid electrolyte preparation.

### 2.1 Solid-state synthesis

One of the most accessible and straightforward routes to obtaining solid electrolytes is by mixing solid precursors and applying heat to drive their reaction. Such synthesis is referred to as “solid-state-”, “high-temperature-” or “ceramic-” synthesis<sup>91</sup> and has led to the synthesis of some of the most highly conducting  $\text{Li}^+$  and  $\text{Na}^+$  solid electrolytes in recent literature. For example, the  $\text{Li}_{6.6}\text{Si}_{0.4}\text{Sb}_{0.6}\text{S}_5\text{I}$ , synthesized from binary reagents *via* solid-state routes, shows  $\text{Li}^+$  conductivity of  $14.8 \text{ mS cm}^{-1}$ .<sup>92</sup> Similarly, the synthesis of the W-doped  $\text{Na}_{2.9}\text{-Sb}_{0.9}\text{W}_{0.1}\text{S}_4$  with a  $\text{Na}^+$  conductivity of  $\sim 40 \text{ mS cm}^{-1}$  was also achieved by solid-state synthesis.<sup>12,27</sup>

**2.1.1. Mechanistic aspects.** The energy input needed to drive the atomic rearrangements and bond-breaking in order to turn the reagents into the products in solid-state routes is purely thermal. As such, the centerpiece equipment for solid-state synthesis is a controlled-temperature environment, *i.e.* a furnace. Despite its simplicity, solid-state synthesis involves a certain number of variable parameters, whose accurate choice and control can dictate the degree of success of the intended reaction as discussed below:

The first step in any solid-state synthesis is ensuring the intimate mixing of the reagent powders, which is crucial given the limited diffusivity of atoms in the solid-state. Since the reactivity of a material varies significantly with particle size, selection of the starting materials itself plays a dominant role.

Table 1 Advantages and disadvantages of discussed solid electrolyte synthesis routes

Method	Advantage	Disadvantage
Classical high-temperature solid-state syntheses	Well-explored; much background knowledge	Bulk material production is time and energy consuming and not suitable for practical use Not suitable for non-equilibrium phase formation
Mechanochemical syntheses	Scalable material production; synthesis of non-equilibrium phases, reduced post synthesis processing time and temperature	Difficult to control the particle morphology. Optimization of processing parameters is needed
Solution syntheses	Scalable, cost-effective approach; synthesis of non-equilibrium phases, reduced post-synthesis processing time and temperature. Possibility controlled particle morphology	Underlying reaction chemistry sometimes poorly understood, as well as interactions between reagents and solvent Solvent choice can be critical but is nontrivial. Solvent residue or carbonized solvent can remain in product
Sol-gel syntheses	Scalable; non-equilibrium phases attainable	Expensive alkoxide routes. Not universally applicable since it is difficult to choose the right alkoxide reagents having similar reactivity for a given stoichiometry
Microwave syntheses	Energy-efficient and cost-effective synthesis process	Not well-optimized; influence on phase formation is not well understood yet
Post-synthetic treatments	Controlled material density, particle size and morphology, crystallinity and associated conductivity	Materials decomposition if the conditions are not carefully monitored



Further, grinding helps to reduce the particle sizes, prepare a homogenous precursor mixture and generate interfaces of physical contact between the reagent powders, all of which help to overcome diffusion limited product particle growth. Such grinding can be performed manually, using a mortar and pestle, or mechanically using a milling machine, typically a ball-mill. In certain cases, mechanical milling alone can drive reactions to completion, referred to as mechanochemical synthesis, which will be discussed specifically in Section 2.2. After grinding, the powder mixtures are typically densified into pellets through mechanical pressing to reduce porosity and thus maximize physical contact between the reagent particles.

The subsequent control of the sample environment can decisively affect the results of solid-state synthesis. The reaction vessel must be chosen to eliminate the possibility of reactivity with the reagents, with typical choices being alumina, silica (quartz), and glassy carbon. Still, either unintended incorporation of chemical species from the vessel or change in stoichiometry of the product due to loss of reagents by reaction on the vessel surface can occur; for example, synthesis of  $\text{Li}_7\text{La}_3\text{Zr}_2\text{O}_{12}$  garnet in alumina crucibles leads to Al-doping, which in itself was the reason for the success of  $\text{Li}_7\text{La}_3\text{Zr}_2\text{O}_{12}$  early on, as it stabilizes the fast conducting cubic phase.<sup>93</sup> For cases of extreme reactivity, refractory materials such as tungsten, tantalum and boron nitride can also be used. For solid electrolytes, noble metal crucibles (*e.g.* gold, silver, platinum) are not preferred due to their reactivity/alloying with the alkali metals and their preferred reaction with sulfides. For example, the synthesis of  $\text{Na}_3\text{PS}_4$  in Au crucibles leads to the formation of  $\text{Na}_3\text{AuS}_2$  side-phase.<sup>94</sup> The ambient atmosphere can be manipulated to promote oxidizing or reducing conditions, typically by introducing  $\text{O}_2$  or  $\text{H}_2$  gases, respectively. For reagents or products that are prone to reaction with ambient air ( $\text{O}_2$ ,  $\text{N}_2$ ,  $\text{H}_2\text{O}$  and/or  $\text{CO}_2$ ), reactions must be carried out under controlled atmosphere, typically under inert gas ( $\text{N}_2$ , He, Ne, Ar) or vacuum. For example, most sulfides will hydrolyze producing  $\text{H}_2\text{S}$  upon exposure to air,<sup>95</sup> and oxides such as the  $\text{Li}_7\text{La}_3\text{Zr}_2\text{O}_{12}$  garnet are prone to protonation by  $\text{Li}^+/\text{H}^+$  exchange and surface carbonation by  $\text{Li}_2\text{CO}_3$  formation,<sup>96–99</sup> which can decrease ionic conductivity by one or more orders of magnitude.<sup>100</sup> Thus, in practice, such manipulations typically involve a glove-box, either featuring a furnace or in combination with a sealable reaction vessel. For Li-ion conducting sulfides, a typical setup involves the sample placed in an evacuated silica ampoule whose interior walls have been coated with carbon through pyrolysis of a solvent such as acetone, or the use of glassy-carbon crucibles.<sup>13,81</sup>

The reaction temperature profile refers to the change of the furnace (and by extension, sample) temperature over time. This includes target temperature(s), annealing time(s) as well as heating and cooling rates. The temperature(s) dictate the state(s) that the reactants and products will pass through, depending on the phase diagrams of the constituent elements. The effects of temperature can be simply understood through the concept of entropy. Higher temperatures tend to favor symmetric, single-phase (*i.e.* solid solution) behavior by promoting disorder and reactant atom diffusivity. This is

especially relevant to ion conductors for which disorder is often desirable. In contrast, lower temperatures tend to favor phase separation through ordering of the atomic constituents. For example, heating a heterogeneous equimolar mixture of  $\text{Li}_3\text{PO}_4$  and  $\text{Li}_4\text{SiO}_4$  will result in a single phase  $\text{Li}_{3.5}\text{P}_{0.5}\text{Si}_{0.5}\text{O}_4$ , where the  $\text{PO}_4^{3-}$  and  $\text{SiO}_4^{4-}$  are randomly distributed, increasing the ionic conductivity by at least three orders of magnitude compared to the end-members.<sup>101</sup> Manipulating such solid solutions is a key strategy in controlling the concentration of charge carriers in an solid and as such tailoring ionic conductivity.<sup>18,101</sup>

In the absence of accurate phase diagrams, important temperatures to consider are phase transitions (typically melting) of the reactants and products. Melting of a reaction mixture can strongly increase reaction rates and facilitate homogeneous mixing of elemental constituents, owing to the much faster diffusion rates in the liquid phase. Nevertheless, melting is not always desirable owing to various possible complications, *e.g.* reactivity with the reaction container, volatilization of the reaction mixture, and incongruent solidification. For example, the high-performance quaternary phase  $\text{Li}_{10}\text{GeP}_2\text{S}_{12}$  will melt incongruently above  $\sim 600$  °C into a phosphorus-rich liquid, from which it is almost impossible to recover a pure phase.<sup>102</sup> Regrettably, construction of phase diagrams and accurate melting point determination are not commonplace in recent solid-electrolyte-related work. The case of  $\text{Li}_{10}\text{GeP}_2\text{S}_{12}$  provides a notable exception; the careful determination of the  $\text{Li}_3\text{PS}_4$ – $\text{Li}_4\text{GeS}_4$  phase diagram,<sup>102</sup> has enabled the rational synthesis optimization as well as the growth of single crystals of this seminal material for in-depth structural and dynamic studies.<sup>103</sup>

The cooling and heating rates can be used to control kinetic effects that might affect a given synthesis. Generally, if the reaction product is thermodynamically favored, low rates and long annealing time are preferred. Lower heating rates also practically help to alleviate the overshoot of temperature that might be experienced by the sample. Long annealing times and slower cooling rates result in better crystallinity by allowing for grain growth (sintering) and the release of mechanical strain induced by lattice contraction during cooling (thermal shock) which can have a severe impact on crystal structure and ion transport. A notable example is that of the  $\text{Li}_7\text{La}_3\text{Zr}_2\text{O}_{12}$ -type garnets<sup>104</sup> and NASICONs<sup>105</sup> that present high intrinsic ionic conductivities of the order of  $\text{mS cm}^{-1}$  in the bulk but typically blocking grain boundaries that decrease the conductivity in polycrystalline pellets. Here, the parameters of the thermal treatment greatly affect the resulting microstructural features (grain size, grain boundaries, phase impurities) which in turn control the final ionic conductivity.<sup>48</sup> In another example, variation of the grain-size of the  $\text{Li}_{0.3}\text{La}_{0.57}\text{TiO}_3$  perovskite in the range 860 to 25 nm through sintering was shown to decrease its ionic conductivity by four orders of magnitude, likely again due to the presence of more blocking grain boundaries.<sup>106</sup>

If the desired product is not thermodynamically favored at temperatures below the reaction temperature, a fast cooling rate can help kinetically stabilizing it, a procedure commonly referred to as quenching. The desired product can be a distinct



crystallographic polymorph or a more disordered arrangement of constituents in a given crystal structure, often quantified by partial occupation of shared sites. While a slow cooling might allow for the ordering of constituents with decreasing temperature, quenching can “freeze” the high temperature configuration if the necessary atomic rearrangements are too slow to occur at lower temperature, even if they are thermodynamically favored. In practice, quenching is typically performed by submerging the reaction container in a cold fluid, typically water, but also oil or liquid nitrogen; even room-temperature air can sometimes be used depending on the reaction kinetics. The higher the heat capacity and thermal conductivity of the quenching fluid, the higher the cooling rate. Such effects have recently been demonstrated for the argyrodite  $\text{Li}_6\text{PS}_5\text{Br}$ , in which the  $\text{S}^{2-}/\text{Br}^-$  site disorder decisively affects ion transport by affecting the dynamics of  $\text{Li}^+$  diffusion.<sup>84</sup> By cooling at different rates and from different temperatures the authors showed that the degree of site disorder could be controlled, with quenching increasing the resulting ionic conductivity fourfold compared to slower cooling.<sup>84</sup> The ability of the reaction vessel to withstand thermal shock is critical; quartz can remain intact through rapid changes over hundreds of degrees, while a quenched ampoule of borosilicate glass might have quite undesirable results.

A final comment that is especially relevant to the solid-state synthesis of ion conductors pertains to the common volatilization of the reagents at high temperature, leading to deviations from the intended stoichiometry of the final product. Typical culprits involve S, O<sub>2</sub>, and Li/Na-precursors, which tend to develop non-negligible vapor pressures. This is prevalent, *e.g.* in the synthesis of  $\text{Li}_7\text{La}_3\text{Zr}_2\text{O}_{12}$ -type garnets where volatilization of Li leads to decrease the final Li content of the material.<sup>104</sup> Such problems are typically empirically alleviated through the addition of excess, “sacrificial” amounts of these reagents, which however requires careful trial and error for stoichiometric control.

**2.1.2. Remaining challenges.** Despite the advantages discussed above, solid-state synthesis suffers from a few drawbacks, mainly linked to upscaling. The lab-scale synthesis in evacuated silica ampules present obvious limitations to the batch size. The long annealing times required and the associated energy expenditure to reach and maintain the high temperature will also need to be considered in economic industrial terms (this can be somewhat alleviated with furnaces maintained at temperature with products moving through, *e.g.* rotary tube furnace). Finally, when the performance of the solid electrolyte hinges on the introduction of certain non-equilibrium features (*e.g.* charged defects and disorder), other synthesis methods might prove more adept to that end, as described below.

## 2.2. Mechanochemical synthesis

Another common synthetic route for the successful production of pure ion conductors is the use of mechanochemistry, which deals with the influence of mechanical energy like compression, shear or friction in chemical and physicochemical

transformations.<sup>69,107–110</sup> Though mechanochemical synthesis (often mentioned as ‘ball milling’) was discovered as a subsection of solid-state synthesis, in recent days it is a widely used synthetic technique in various fields including metal-organic frameworks, biomaterials, catalysts, organics, and pharmaceuticals.<sup>111</sup> The hallmark of this method includes the application of mechanical force controlling the reactivity of solids by the evolution of crystal defects, interphases, and tuning the relaxation phenomena, where materials can be effectively ground, amorphized, and mixed. Thus, it facilitates the reactions to occur under non-equilibrium conditions.<sup>107,112,113</sup> This brings several technological successes including synthesis of non-equilibrium phases with the desired dimension, enhanced concentration of vacancies, formation of crystal defects, a striking reduction of crystallization temperature and post-synthetic annealing time duration which ultimately gives the choice to tune their transport, reproducibility, high production yield and efficient utilization of energy and materials under basic operating conditions.<sup>69,84,114</sup> For Li-ion conductors, defects are required for long-range ion conduction. Thus, mechanochemical synthesis is a well-known route used for the synthesis of Li-ion conducting sulfide glass electrolytes. The synthesis of crystallized ion conductors involves amorphous phase formation *via* ball milling followed by an additional annealing step.<sup>15,115,116</sup> The mechanochemical synthesis of garnet-like Li-ion conductors offers a significant reduction of annealing temperature and time.<sup>113</sup> The synthesis of superionic argyrodites ( $\text{Li}_6\text{PS}_5\text{X}$ , X = Cl, Br, I) requires much lower crystallization time as compared to material synthesized by usual diffusion-mediated solid-state synthesis.<sup>117,118</sup> Furthermore, it is a common route to prepare nano-dimensional heterostructured ion conductors.<sup>119</sup> Improved interfacial ion diffusion has been realized in nanocrystalline  $\text{Li}_2\text{O}-\text{X}_2\text{O}_3$  heterostructure when  $\text{Li}_2\text{O}$ , an ion conductor and ionic insulator  $\text{X}_2\text{O}_3$  (X = Al, B) were mechanochemically mixed.<sup>120</sup> Mechanochemically-synthesized halide-substituted  $\text{LiBH}_4$  ( $\text{Li}_4(\text{BH}_4)_3\text{I}$ ) has shown superior conductivity.<sup>121</sup> Recently, ternary metal halides have been rediscovered as promising solid electrolyte candidate when prepared *via* mechanochemical route.<sup>69,122</sup>

**2.2.1. Mechanistic aspects.** The impact of mechanochemical transformation is driven by the amount of energy transferred during mechanical interaction between the sample particles and working media to alter the chemical reactivity of the sample.<sup>107</sup> Planetary ball mill and mixer (shaker) mills are the two main instruments used for this process and for an in-depth description of mechanical milling we refer the reader to the review by Kwade and Burmeister.<sup>108</sup> In the planetary mill, the milling media (*i.e.* milling balls) and reactants undergo two types of movements (Fig. 2). Friction with the inside walls of the vessel because of the centrifugal force resulting from revolution of vessel against the center of the mill, and its effect when they lift off and collide with the opposite wall due to rotation. In case of shaker mills, the horizontally placed milling vessel can swing back and forth, and thus induces the collision between milling media and/or reactants and the opposite wall of the vessel. This process is usually defined as high-speed ball milling or high-speed vibration milling. Due to the efficient energy utilization,



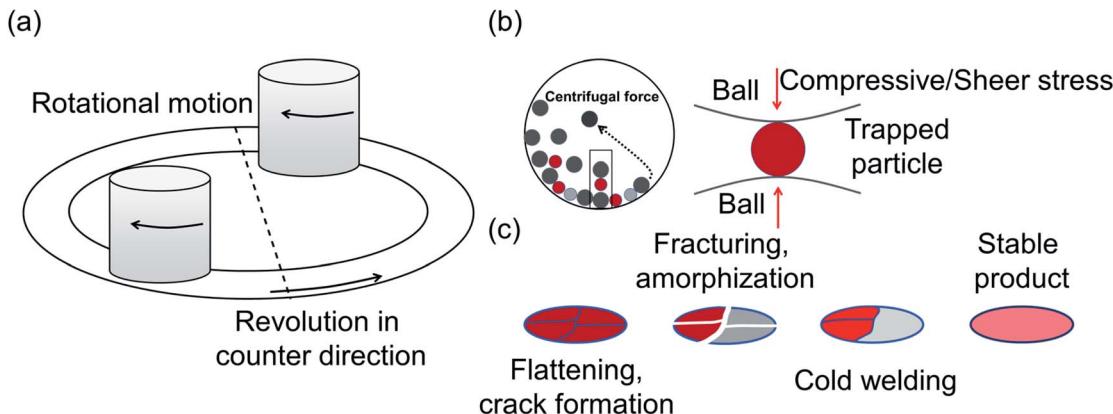


Fig. 2 (a) Schematic diagram for the planetary ball-mill showing movement of a milling vessel and planetary disks in a clockwise and counter clockwise direction. (b) A simplified view showing motion of the milling balls (dark gray) and sample particles (red and light gray) mixture inside the mill generating compressive stress. Mechanical energy generated during their interaction results in the material transformation. (c) Steps of evolution of sample particle during mechanochemical synthesis – flattening, fracturing, welding and stable end product formation.

simple set-up, ease of handling and cleanability, planetary ball mills have been adopted in the ionics community.<sup>109</sup>

The important variables which influence the milling process include type of the mill, nature of milling media (size, mass, mechanical strength and chemical composition), milling media-to-sample ratio, filling extent of the milling chamber, milling atmosphere, milling speed at a constant speed ratio, milling time, *etc.* These variables can alter the nature of impacts like the stress frequency, the stress energy and also the amount of trapped powder in-between colliding bodies, which eventually control the energy transfer by varying these above mentioned parameters. The total amount of energy transferred to the product particles during the milling process can be estimated based on the following expression, where  $\Delta SF_j$  is the frequency of stress events at interval  $j$ ,  $SE_j$  is the average stress energy and  $t$  is the processing time. Hence, the total energy can be represented as the product of the total number of stress events  $SN$  and the average stress energy  $\overline{SE}$ . The specific energy  $E_i$  is the ratio of the total energy to the total mass of the powder,  $m_p$ .<sup>108</sup>

$$E_i = \frac{\sum_{j=1}^n SE_j \Delta SF_j}{m_p} \times t = \frac{SN \times \overline{SE}}{m_p} \quad (1)$$

The stress energy  $SE$  is the maximum amount of energy that can be transferred to the product particles during single collision. This can be calculated from the relative impact velocity  $v_j$  and the masses of the colliding bodies  $m_1$  and  $m_2$  as given below:<sup>108</sup>

$$SE = \frac{v_j^2 m_1 m_2}{2(m_1 + m_2)}. \quad (2)$$

The choice of the material used in milling balls is governed by its thermal stability, nature of interaction with the sample powder to prevent product degradation *via* secondary reactions or cause abrasion and damage the milling vessel.<sup>108</sup> Agate,

silicon nitride, sintered corundum, zirconia, chrome steel, Cr-Ni steel, tungsten carbide, or polyamide are the typical materials used in the mechanochemical vessels and milling media. Use of zirconia milling balls has proven to be more effective for the synthesis of sulfur based glass-ceramic electrolytes.<sup>123</sup> Furthermore, it is recommended to use milling media with a uniform diameter to avoid a random motion of the balls without well-defined trajectories in the vessels. Milling balls with a large diameter and/or larger mass provide higher impact energy during the collision and, therefore, are suitable for reactions where particle refinement can enhance the surface activity.<sup>108</sup> In addition, a larger milling vessel leads to higher kinetic energy being transferred.<sup>108</sup> However, a higher density of milling media can generate high stress which can cause degradation of the reaction product because of the local heating.

Milling media-to-sample ratio and the degree of filling of the milling vessel play a critical role in the milling process. At a constant density and diameter, the quantity of milling media controls the reaction rate by altering the stress number,  $SN$ . Thus, to obtain a specific reaction yield, the required amounts of milling media depends on both the diameter and number. Although the reaction yield and quantity of milling media shows a linearly proportional behavior for any chemical synthesis upto a certain limit, the use of an excessive amount of milling media will result in a poor yield due to their constrained movement inside the loaded vessel.

One of the essential parameters for synthesis optimization is the milling speed that determines the amount of energy transfer for given masses of the colliding bodies during the milling process.<sup>107</sup> The energy is supplied to the particles due to collisions with the milling balls. Although it is difficult to gauge the actual mechanism of ball milling because of its complex nature, the internal process can be visualized as follows: during high-energy milling, the particle size of the materials decreases to a critical value; an additional supply of energy to these materials of limiting size seeds deformation, enhanced surface



reactivity, and subsequently amorphization. It eventually leads to change in the surface area, particle size, reaction kinetics, phase transformations, atomic defects formation and non-equilibrium product formation. For instance, in order to synthesize the argyrodite  $\text{Li}_6\text{PS}_5\text{X}$ , the use of mechanical milling as a preliminary step allows rapid reactions of  $\text{Li}_2\text{S}$  with  $\text{P}_4\text{S}_{10}$  to form *ortho*-thiophosphate and probable nucleation clusters of  $\text{Li}_6\text{PS}_5\text{X}$ ; this bypasses the normally long diffusion-mediated reaction.<sup>84</sup>

The primary nature of responses to mechanical action are (a) redistribution of cations/anions over non-equivalent crystallographic sites,<sup>69,84</sup> (b) changes in the geometry of constitutive polyhedra which significantly alter the ion migration entropy<sup>69</sup> and activation energy of transport, further discussed in Section 3.3, (c) formation of crystal defect<sup>112</sup> and (d) the mechanically induced phase transformation.<sup>81</sup> During the high-energy ball milling process, a material undergoes a continuous fragmentation and deformation process, resulting in the reduction of their crystallite size. By this comminution, many nanocrystalline ion conductors were prepared, which showed improved transport properties, for example ternary fluorides show greatly enhanced ionic conductivity.<sup>124</sup> Recent studies show an effective change in conductivity of c- $\text{Na}_3\text{PS}_4$ , which can be attributed to a combination of crystal defect formation and its nanocrystalline nature as (discussed in Section 3.1).<sup>75</sup>

Another important parameter is milling time. The yield increases with milling time due to the gradual rise in the collision number and the total energy transfer. Wagemaker's group reports significant impact of milling time on the Li-ion mobility of  $\text{Li}_6\text{PS}_5\text{Br}$ , which is associated with distribution of  $\text{Br}^-$  ion over different crystallographic sites.<sup>125</sup> Meng and coworkers have thoroughly studied the influence of milling time on the ionic conductivity of  $\text{Na}_3\text{PS}_4$ .<sup>126</sup> With increasing milling time conductivity increases and reaches a maximum value of  $\sim 0.2 \text{ mS cm}^{-1}$  within 1 hour; the ionic conductivity does not increase further with additional milling process indicating completion of the reaction. Rapid production of high conducting  $\text{Na}_3\text{PS}_4$  confirms the role of ball milling as a promising alternative to other existing energy-intensive multiple-step methods. However, prolonged ball milling can lead to formation of undesired material due to the decomposition the reaction product.<sup>127</sup>

**2.2.2. Remaining challenges.** Although in recent time we have seen rapid growth on the development of ionic conductors with improved properties based on mechanochemical synthesis, it is hard to set good assessment parameters for ball milling processes on the crystal structure and associated Li-ion conduction because of its complex mechanism. To date, most milling studies are purely based on experimental trial and error optimization of milling conditions, whereas the known influences that industrial engineers have developed over the past decades are often neglected.<sup>108</sup> Thus, to understand the actual influence of this process on superionic conductors, further thorough systematic studies are necessary. Additionally, similar to typical solid-state synthesis, it is difficult to control the morphology of solid electrolytes *via* ball milling, a factor that drives the motivation for solution-based synthesis or solution

processing as discussed in the following section. However, with that said, it is hopefully obvious from the aforementioned overview that mechanochemical synthesis has progressed far from being a "black-box" process, with much work having been done to more carefully understand and control the complex interplay of variables.

### 2.3. Solution-assisted synthesis

Solvent processes are attractive, whether as a synthetic medium (alone or in conjunction with other techniques such as milling), or as processing medium such as suspension/dissolution and infiltration of electrolyte.<sup>65</sup> Solvents are sought according to a number of criteria. We have categorized solution mediated synthesis of solid electrolyte in two sections. This section will be focused on thiophosphate materials whereas in the next section, we will briefly discuss oxide electrolyte processing. For the syntheses of lithium-ion conducting thiophosphate solid electrolytes, the paradigm to date is typically reaction of  $\text{Li}_2\text{S}$  with  $\text{P}_4\text{S}_{10}$  at varied stoichiometry, with the possible addition of extra  $\text{Li}_2\text{S}$  and lithium halides ( $\text{LiX}$ ;  $\text{X} = \text{Cl}, \text{Br}, \text{I}$ ) for more complex compositions.<sup>65,83,128,129</sup> For the purpose of this summary, the formula  $\text{P}_2\text{S}_5$ , due to its prominence in the literature, is sometimes used interchangeably with  $\text{P}_4\text{S}_{10}$ , although the compound actually consists of isolated cage-like molecules of  $\text{P}_4\text{S}_{10}$ ,<sup>130</sup> further, it should be noted that commercial  $\text{P}_4\text{S}_{10}$  is generally high in impurities of  $\text{P}_4\text{S}_9$  and possibly polysulfidic species, which are much higher in reactivity.<sup>131</sup> The reactants typically do not fully dissolve and a heterogeneous reaction system is the norm.

**2.3.1. Mechanistic aspects.** It should be noted here that the resulting products of reaction are quite sensitive to the stoichiometry of  $\text{Li}_2\text{S} : \text{P}_4\text{S}_{10}$ . Small changes can result in large differences of the species distribution present:  $\text{PS}_4^{3-}$ ,  $\text{P}_2\text{S}_6^{2-}$ ,  $\text{P}_2\text{S}_7^{4-}$ ,  $\text{P}_2\text{S}_6^{4-}$ ,  $\text{S}_0/\text{S}-\text{S}$ .<sup>65,87,123,132,133</sup> This can also apply locally; 75 : 25  $\text{Li}_2\text{S} : \text{P}_2\text{S}_5$  (typical stoichiometry for  $\text{Li}_3\text{PS}_4$ ) under certain conditions in acetonitrile (ACN) resulted in  $\text{Li}_7\text{P}_3\text{S}_{11}$  with  $\text{Li}_2\text{S}$ , likely the result of local stoichiometry closer to 70 : 30 due to unreacted  $\text{Li}_2\text{S}$ .<sup>134</sup> Thus incomplete reaction and uncontrolled heterogeneous distribution of reactants can be a potential pitfall in synthesis. There seems to be no ideal solvent that fully dissolves starting materials and/or products without inducing unwanted reactions (thus making isolation of products difficult) – alcohols such as ethanol may dissolve  $\text{Li}_2\text{S}$  and  $\text{LiX}$ , but may tend to attack and decompose  $\text{P}_4\text{S}_{10}$ .<sup>130</sup> This may also be a problem with *N*-methyl formamide (NMF), as suggested by Tatsumisago and coworkers; in this case the reaction was performed in a mixture of NMF and hexane to mitigate undesired reactivity.<sup>57</sup> Further, some compositions are difficult to synthesize in a single solvent. Argyrodites, *e.g.*  $\text{Li}_6\text{PS}_5\text{X}$  ( $\text{X} = \text{Cl}, \text{Br}, \text{I}$ ), do not form in tetrahydrofuran (THF) from binary precursors due to the stability of precipitated  $\text{Li}_3\text{PS}_4$  and insolubility of other reactants, and the overall reaction also does not proceed satisfactorily in ethanol alone, likely due to the aforementioned restrictions. Therefore, an approach of first forming  $\text{Li}_3\text{PS}_4$  (to eliminate the possibility of attack of  $\text{P}_4\text{S}_{10}$ ) and subsequent addition of  $\text{Li}_2\text{S}$  and  $\text{LiX}$  was utilized; either by



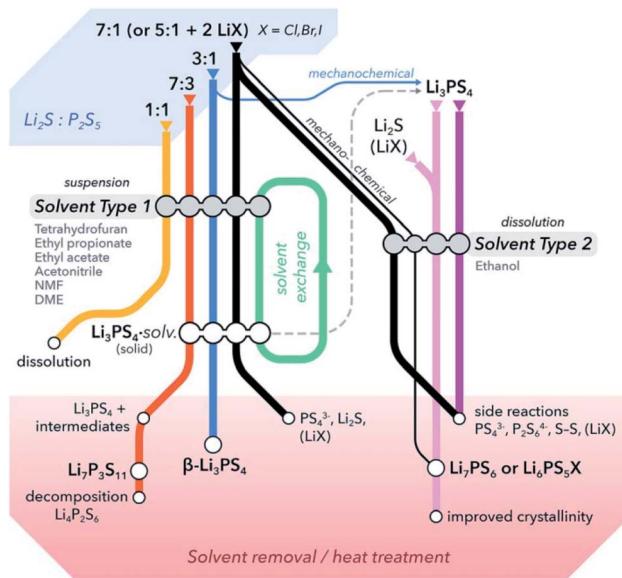


Fig. 3 A general overview of literature reported solution routes for the synthesis of common thiophosphate solid electrolytes. Based on the choice of solvents, reaction steps, and post-synthetic heat treatments, it is possible to prepare thiophosphates with different compositions, structures or morphologies using  $\text{Li}_2\text{S}$ ,  $\text{P}_2\text{S}_5$  and/or  $\text{LiX}$  as preliminary precursors. Solvents are differentiated into two types based on their properties such as polarity, donor number, etc.; DME stands for dimethyl ether. This figure is adopted from ref. 65.

initial reaction in solvent to produce  $\text{Li}_3\text{PS}_4$ ,<sup>135,136</sup> or by starting with  $\text{Li}_3\text{PS}_4$  produced by solid-state means.<sup>55</sup> Later, some success was realized with  $\text{Li}_6\text{PS}_4\text{Cl}$  in ethanol alone using  $\text{Li}_2\text{S}$ ,  $\text{LiCl}$  and  $\text{P}_2\text{S}_5$ , albeit with a conductivity lower than expected.<sup>54</sup>  $\text{Li}_3\text{PS}_4$  was shown to first crystallize as a complex with solvents it was synthesized in, such as THF and acetonitrile; this will be discussed later in Section 3.3. On a final note, there is clearly chemistry that is not yet fully understood, as there are reports of mixtures of 1 : 1  $\text{Li}_2\text{S} : \text{P}_2\text{S}_5$  dissolving in solvents that neither reactant dissolves in.<sup>65</sup> Fig. 3 summarizes a generalized reactivity trend in the  $\text{Li}_2\text{S}-\text{P}_2\text{S}_5-(\text{LiX})$  system in solution.

**2.3.2. Remaining challenges.** Regardless of the synthetic route, electrolytes can have different behaviors when

introduced into solvents: (a) there could be no reaction at all, (b) non-dissolution accompanied by some degree of reaction, (c) simple dissolution, (d) dissolution by means of reaction, or (e) unrecoverable degradation. Overall, the underlying reaction pathways for making ionic conductors *via* solution routes are not fully understood and the design of synthesis for fast ionic conductors *via* solvent routes is still in need of being able to reproducibly produce fast ionic conductors.

#### 2.4 Sol gel syntheses

Sol-gel routes have emerged as an energy efficient alternative of solid-state synthetic technique to prepare inorganic ceramics from homogenized solution *via* formation of a network structure called 'gel'.<sup>137</sup> The advantage of sol-gel synthesis relies on the successful preparation of solid-state compounds from a chemically homogeneous precursor solutions. It is a well-established route to prepare oxide- and phosphate-based ionic conductors such as the garnets, LISICONs, and NASICONs.

**2.4.1 Mechanistic aspects.** A typical sol-gel process can be summarized in the following steps (Fig. 4): (a) preparation of metal alkoxides by dissolving metal chloride or nitrate salt in alcohol; (b) hydrolysis and partial condensation of metal alkoxides to form colloidal suspension which is termed as 'sol'; (c) gel formation *via* polycondensation to form metal-oxo-metal (M-O-M) bonds; (d) 'aging', *i.e.* condensation within the gel network, resulting in removal of solvent; (e) drying the gel to form a dense 'xerogel'; (f) calcination for complete removal of surface M-OH groups. Since hydrolysis and condensation are the basis of sol-gel synthesis, only metal alkoxide having similar reactivity towards hydrolysis can be only used for ternary compound formation. The reactivity of the alkoxides for a typical sol-gel reaction depends on various parameters. Electronegativity differences between the oxygen and metal determines the ionic character of the M-O bond. Inductive effects of the alkyl/aryl chain influences the stability of the alkoxy groups.<sup>138</sup> Furthermore, a slight change in the precursor solution can influence calcination temperature and product morphology. Aqueous-based sol-gel syntheses were employed to prepare highly conducting ( $0.69 \text{ mS cm}^{-1}$ )  $\text{Li}_{1.5}\text{Al}_{0.5}\text{Ti}_{1.5}(\text{PO}_4)_3$  from  $\text{Al}(\text{C}_3\text{H}_7\text{O})_3$ ,  $\text{Ti}(\text{C}_3\text{H}_7\text{O})_4$  and  $\text{CH}_3\text{COOLi}$  in ethanol-

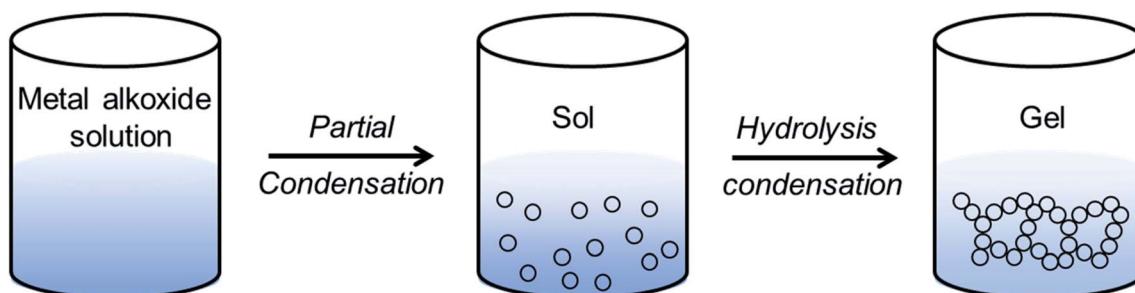


Fig. 4 Schematic of sol-gel synthesis used for the ceramic materials. Metal alkoxide ( $\text{M}-\text{O}-\text{R}$ ; where R is alkyl or aryl group) is formed via dissolution of metal salts in alcohol. Hydrolysis and partial condensation of metal alkoxide leads to 'sol' formation, which upon further heating undergoes polycondensation to form a three-dimensional gel network. The gel can be transformed into powdered product upon high temperature decomposition and calcination.

water mixture; however, the use of  $\text{Al}(\text{NO}_3)_3$  as aluminium source leads to formation of  $\text{AlPO}_4$  as secondary phase originating from improper mixing of reagents and thus results in lower ionic conductivity.<sup>139</sup>

The major limitation of alkoxide-based sol-gel chemistry is that it is difficult to get a stable metal-alkoxide.<sup>137</sup> To overcome this drawback, an alternative method has been developed that uses aqueous metal salts precursor and small molecules as chelating agents to tune the aqueous hydrolysis process of metal alkoxide. One of the most common chelating agents used in sol-gel chemistry is citric acid. In a modified sol-gel synthesis, the homogenized solution of aqueous metal salts (mostly nitrates) and citric acid is heated to form gel. Murugan's group prepared Al-doped cubic phase of LLZO,  $\text{Li}_{6.16}\text{Al}_{0.28}\text{La}_{3.7}\text{Zr}_2\text{O}_{12}$  (Al-LLZO) by a modified sol-gel technique.<sup>140</sup>

When carboxylic acids (like citric acid, tartaric acid, polyacrylic acid, *etc.*) are used as chelating agents along with polyhydroxy alcohol (such as ethylene glycol, glycerol, polyvinyl alcohol, *etc.*), the modified sol-gel method is termed as Pechini process.<sup>137</sup> Here, the metal carboxylates undergo polyesterification upon heating and form a three-dimensional network of polymeric resin. The cations are then homogeneously dispersed all over the polymeric resin, thus inhibiting the precipitation. The low temperature calcination of resin yields nano dimensional oxide. Fang's group prepared nanocrystalline cubic phase of lithium garnets,  $\text{Li}_5\text{La}_3\text{Ta}_2\text{O}_{12}$  and  $\text{Li}_5\text{La}_3\text{Bi}_2\text{O}_{12}$  *via* the Pechini sol-gel method by calcining the gels at 700 °C and 650 °C, respectively.<sup>141,142</sup>

**2.4.2 Remaining challenges.** Sol-gel synthesis is a powerful tool to prepare industrial scale oxide electrolytes. The choice of precursor has strong influence on the ultimate product, its purity, density and eventually the transport properties. Thus, studies are needed to gain a better understanding of how molecular precursors influence the sol-gel process, particularly molecular interactions during the gelation procedure. In

addition, it may be worthwhile to explore sol-gel chemistry in the preparation of sulfide materials.

## 2.5 Microwave synthesis

Microwave syntheses of solid-state inorganic materials have emerged with the goal of energy-efficient and cost-effective synthesis by reducing the reaction time and heating temperature.<sup>143</sup> It offers potential solutions for industrial applications and also a means to access metastable materials, which draws the attention of materials chemists. In the case of battery materials, numerous electrode materials, *e.g.* intercalation-type cathodes<sup>144–146</sup> and carbon-based anodes,<sup>147,148</sup> have been synthesized *via* microwave methods.<sup>149</sup> Despite the emerging use of the microwave synthesis in various fields, there are only a few reports on the successful synthesis of solid electrolytes. In this section, we briefly summarize the technical requirements and unique nature of microwave-assisted synthesis and applications to the synthesis of solid electrolytes.

**2.5.1. Mechanistic aspects.** The use of microwave irradiation for synthesizing inorganic materials became widespread after the discovery of strong absorption of microwave in some oxide materials (*e.g.*  $\text{ZnO}$ ,  $\text{V}_2\text{O}_5$ ,  $\text{MnO}_2$ , and  $\text{WO}_3$ ), enabling a rapid temperature rise exceeding 700 °C within a minute.<sup>150</sup> A material-specific microwave absorption relies heavily on its permittivity and dielectric loss, as well as the selected microwave frequency and temperature. For instance, consumer microwave ovens typically use a 2.45 GHz frequency to effectively heat water; however, the dielectric loss becomes about one-third at 90 °C, due to the blueshift of the coupling frequency.<sup>151</sup> Fig. 5a shows a schematic of temperature as a function of microwave time for three different types of materials. Water, graphitic carbon, and SiC are typical MW absorbing susceptors (blue trace). The housing materials should be microwave-transparent and not well-coupled with microwave radiation (yellow trace). Many materials of interest

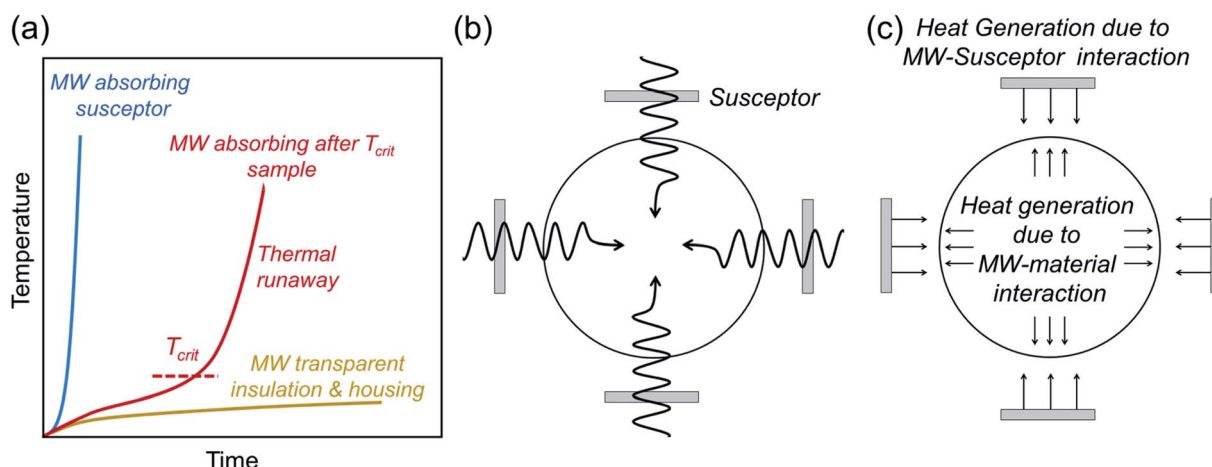


Fig. 5 (a) Schematic of the heating profile of microwave (MW) susceptors, insulators, and the materials possessing critical temperature ( $T_{\text{crit}}$ ) where the microwaves start coupling with the target sample.<sup>153</sup> (b and c) show schematics of heating mechanisms of microwave-assisted synthesis. Whereas only the susceptors are heated up below  $T_{\text{crit}}$ , the heat generation also occurs within the sample above  $T_{\text{crit}}$  due to the coupling with microwave radiation, homogenizing the temperature profile throughout the sample.<sup>154</sup> Figures are redrawn after ref. 153 and 154 respectively with permission. Copyright 2019 American Chemical Society; Copyright 2016 Elsevier.



are not well coupled with microwave radiation until the sample temperature reaches a critical temperature  $T_{\text{crit}}$  (red trace). Therefore, susceptor materials are required to activate such samples to achieve initial heating under microwave irradiation (Fig. 5b). Once the samples are activated, the microwave energy will be effectively transmitted directly to the samples, and there is no need to heat up the entire furnace (Fig. 5c). This leads to inherently low required energy for syntheses, as well as a small thermal mass enabling a rapid temperature ramping. Furthermore, the technique can heat samples fairly homogeneously, whereas a thermal gradient from the sample surface to the interior exists in classic solid-state syntheses, resulting in inhomogeneous heating.<sup>143</sup> For more detail on the mechanistic understanding of microwave methods in solid-state syntheses, we refer the readers to recent summaries by Kitchen *et al.*,<sup>152</sup> Levin *et al.*,<sup>153</sup> and Bhattacharya *et al.*<sup>154</sup>

The first few successful uses of microwave-assisted synthesis for solid electrolytes have been demonstrated with Li-ion conducting oxides. Amores *et al.* synthesized  $\text{Li}^+$  conducting garnets ( $\text{Li}_{6.5}\text{Al}_{0.25}\text{La}_{2.92}\text{Zr}_2\text{O}_{12}$ ) with a microwave method for the first time in 2016.<sup>42</sup> The SiC walls of the microwave furnace can absorb microwaves and initially heat the precursors and  $\text{ZrO}_2$  in the powder as a precursor absorbs microwave above 800 °C.<sup>155</sup> Later Gao *et al.* compared the garnets prepared by microwave-assisted synthesis with those prepared *via* conventional sintering, confirming the lower loss of volatile materials during microwave synthesis.<sup>43</sup> Another Li-ion conducting oxide,  $\text{Li}_{1.3}\text{Al}_{0.3}\text{Ti}_{1.7}(\text{PO}_4)_3$ , was synthesized with a microwave-assisted reactive sintering by Hallopeau *et al.*<sup>156</sup> This work demonstrated a successful preparation of dense pellets within 10 minutes at 890 °C exhibiting over 0.3 mS cm<sup>-1</sup>, which highlight the energy-efficient sintering with a microwave method.

Microwave methods also enable energy-efficient synthesis of Li-ion conducting sulfides *e.g.*  $\beta\text{-Li}_3\text{PS}_4$  and  $\text{Li}_7\text{P}_3\text{S}_{11}$ . Whereas the synthesis of Li-thiophosphate glass and glass-ceramics *via* mechano-chemical alloying or melt quenching often takes 1–3 days,<sup>87,157,158</sup> Suto *et al.* prepared  $\beta\text{-Li}_3\text{PS}_4$  within 3 hours by applying microwave radiation during solution processing.<sup>159</sup> The significant reduction in the reaction time with a microwave-assisted synthesis without solvent was demonstrated by Preefer *et al.* In their work, a successful synthesis of glass and glass-ceramic  $\text{Li}_7\text{P}_3\text{S}_{11}$  was achieved within 18 and 28 min, respectively, with only a minimal amount of the undesirable  $\text{Li}_4\text{P}_2\text{S}_6$  phase.<sup>160</sup> Activated charcoal was employed as a microwave susceptor for the initial heating step. The glass-ceramic  $\text{Li}_7\text{P}_3\text{S}_{11}$  phase is metastable and typically obtainable only through annealing the amorphous 70Li<sub>2</sub>S–30P<sub>2</sub>S<sub>5</sub> glass phase at around 260 °C; thus the direct one-step synthesis of this glass-ceramic  $\text{Li}_7\text{P}_3\text{S}_{11}$  is remarkable.<sup>161</sup> Although the sulfide electrolytes synthesized *via* microwave-assisted synthesis exhibit slightly lower conductivity (0.1 and 1 mS cm<sup>-1</sup> for  $\beta\text{-Li}_3\text{PS}_4$  and glass-ceramic  $\text{Li}_7\text{P}_3\text{S}_{11}$ ),<sup>159,160</sup> this energy-efficient and rapid synthesis method may pave the way for the cost-effective production of highly conductive Li-thiophosphate phases.

**2.5.2. Remaining challenges.** Overall, microwave-assisted synthesis is a promising route for the preparation of ionically conducting solids. Nevertheless, besides a few key experimental

demonstrations there is no detailed report that discusses the mechanistic aspects of the beneficial influence of the fast synthesis time on the bulk ionic transport, nor how it influences grain boundaries, local compositional effects and even phase formation of the ionic conductors.

### 3. Case studies of the influence of synthesis on the structure and ionic transport

In the previous section we summarized synthesis routes typically employed for the production of solid ionic conductors. In this section we will delve deeper into the influence of these different synthesis conditions on structure and ionic transport properties with specific examples, used as case studies, of several inorganic solid electrolytes. We have chosen some of the most well-known solid electrolytes including electrochemically stable garnets and phosphates, Na/Li-conducting thiophosphates, and the recently rediscovered ionically conducting ternary halides. These case studies will highlight the need to understand the influence of synthetic procedures on the local structure, defect formation, phase stability and ultimately the ionic transport properties, in order to tailor production methods to obtain the desired results.

#### 3.1 Milling induced defect introduction and structural stabilization of $\text{Na}_3\text{PS}_4$

Sodium thio-*ortho*-phosphate,  $\text{Na}_3\text{PS}_4$ , is an archetypal Na ion conductor, defining a structural family that includes multiple other notable members such as  $\text{Na}_3\text{SbS}_4$  (ref. 66–68 and 162) and the highly conductive tungsten-doped  $\text{Na}_{3-x}\text{Sb}_{1-x}\text{W}_x\text{S}_4$ .<sup>12,27</sup> Compounds of the  $\text{Na}_3\text{PS}_4$  archetype exhibit a tetragonal ground state and transformation to a closely related cubic polymorph at elevated temperature,<sup>163</sup> owing to convergence of the *a* and *c* lattice parameters and a slight tilting of the constituent  $\text{PS}_4^{3-}$  tetrahedra. For  $\text{Na}_3\text{PS}_4$  this tetragonal-to-cubic transition normally occurs at approximately 250 °C.<sup>164</sup>

Interest in this material family as solid electrolytes boomed after the seminal reports of Hayashi *et al.* showing that the conductivity of  $\text{Na}_3\text{PS}_4$  could reach the order of 0.1 mS cm<sup>-1</sup> through a mechanochemical synthesis route.<sup>26,165</sup> This was a significant improvement over the previous reports of solid-state-synthesized *t*- $\text{Na}_3\text{PS}_4$  (HT- $\text{Na}_3\text{PS}_4$ ), showing  $\text{Na}^+$  conductivity of the order of  $10^{-3}$  mS cm<sup>-1</sup>.<sup>164</sup> Most interestingly, the mechanochemically-synthesized sample exhibited a cubic average structure of the high-temperature polymorph, as evident from Bragg X-ray diffraction (XRD) shown in Fig. 6a (BM- $\text{Na}_3\text{PS}_4$ ). Naturally, the hypothesis was put forward that the stabilization of the high-temperature polymorph through mechanochemistry was responsible for the stark increase in ionic conductivity.

Nevertheless, subsequent theoretical investigations of the ion migration mechanism in the two polymorphs showed that the differences in ion diffusion imposed by the crystal structure alone should be negligible.<sup>94,166–169</sup> On the contrary, these simulations performed by multiple groups indicated that the

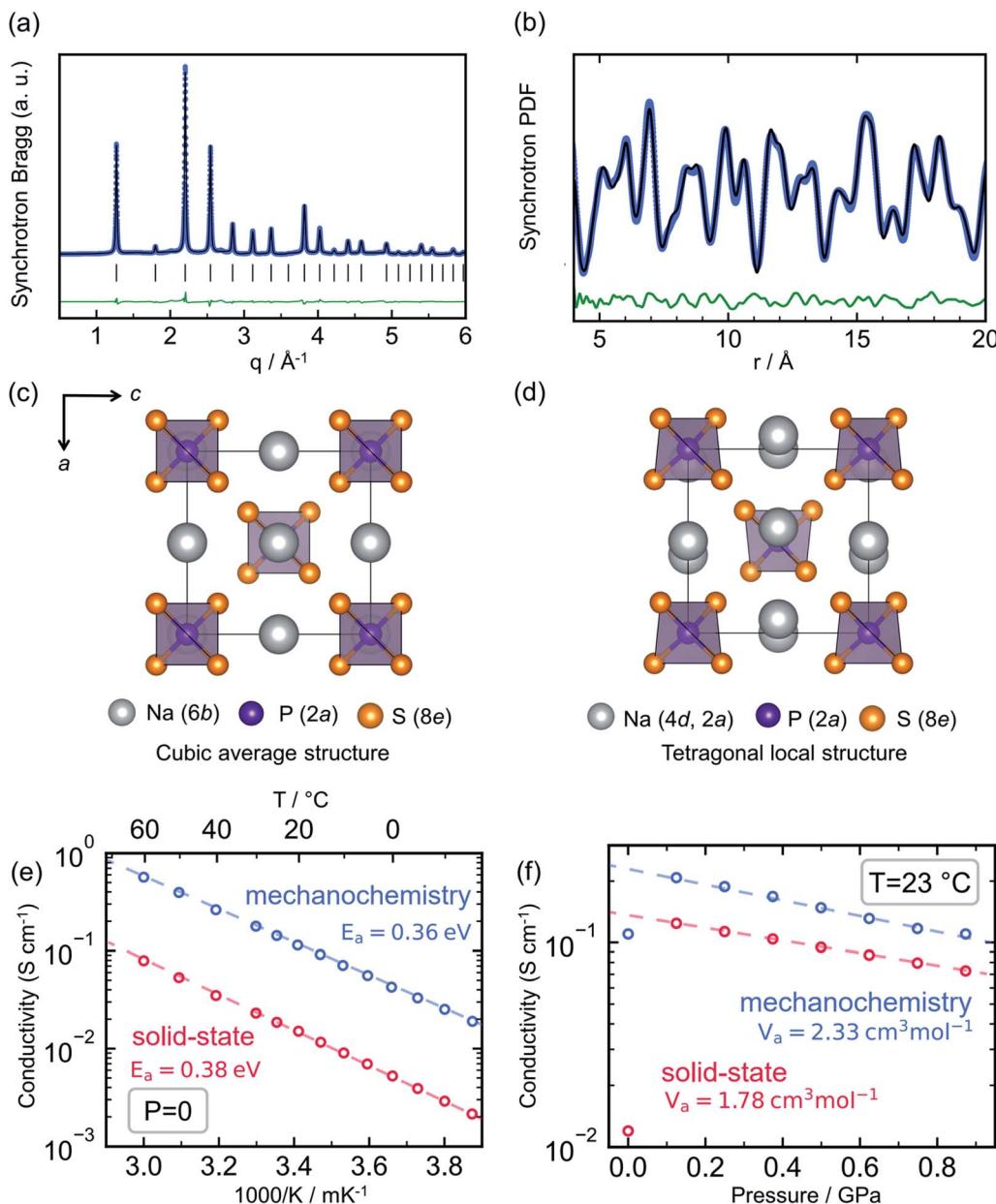


Fig. 6 Mechanochemistry induced local structural distortion in  $\text{Na}_3\text{PS}_4$  and its influence on the ionic conductivity. (a) Powder X-ray diffraction pattern for  $\text{Na}_3\text{PS}_4$  synthesized via ball milling suggests a cubic structure, whereas (b) a local tetragonal distortion was observed in the pair distribution function analyses. Representation of the resulting structural models (c) cubic and (d) tetragonal showing the difference in Na-sublattice. Variation of ionic conductivity for ball-milled cubic- and high temperature-tetragonal phase of  $\text{Na}_3\text{PS}_4$  with temperature and pressure, quantified by their respective activation energy,  $E_a$  and volumes,  $V_a$  are given in (e and f), respectively. Data digitized from ref. 70 and 75.

ion conductivity in the  $\text{Na}_3\text{PS}_4$  structure can be severely affected by the presence of extrinsic defects, such as sodium vacancies and interstitials. Investigations of the local structure by means of total scattering experiments were needed to bring full clarity; studies of BM- $\text{Na}_3\text{PS}_4$  through pair distribution function analysis showed that it possesses the same local tetragonal distortion as HT- $\text{Na}_3\text{PS}_4$ , despite its average cubic symmetry (Fig. 6b).<sup>75,112</sup> The samples are indistinguishable through Raman spectroscopy, due to the same distortions of the  $\text{PS}_4^{3-}$  tetrahedra (which should not be observable in a truly cubic local structure).<sup>75</sup> The  $^{23}\text{Na}$  NMR resonance of BM- $\text{Na}_3\text{PS}_4$  shows clear

signs of isotropy and motional narrowing, indicating higher  $\text{Na}^+$  mobility compared to HT- $\text{Na}_3\text{PS}_4$ .<sup>75,168</sup> Through the aforementioned observations it has been reasoned that the mechanochemical synthesis significantly impacts the sodium sublattice with a positive effect on ion migration. One hypothesis is that the harsh ball-milling conditions induce defects into the crystal structure, possibly  $\text{Na}^+$  vacancies and/or interstitials, along with microstructural strain, which could explain the observed increase in ionic conductivity.<sup>75,112</sup>

Recent experimental results have shown that HT- $\text{Na}_3\text{PS}_4$  can reach a similar order of magnitude in conductivity to BM-

$\text{Na}_3\text{PS}_4$ , through application of external uniaxial pressure, as seen in Fig. 6f.<sup>75</sup> This would indicate that the beneficial effect of ball-milling on the resulting ionic conductivity of  $\text{Na}_3\text{PS}_4$  is related to the mechanical strain generated during the mechanochemical synthesis. *Ab initio* calculations as a function of pressure show that the stabilization of the cubic polymorph can be explained through residual strain. Further, from diffraction experiments, it is evident that BM- $\text{Na}_3\text{PS}_4$  possesses a distinct micro- and macro-strained local structure and minute crystallite size of the order of 25 nm, in stark contrast to the well-crystallized HT- $\text{Na}_3\text{PS}_4$ .<sup>70,75</sup> Such microstructural effects have been hypothesized to aid ion conduction in other mechanically soft solid electrolytes, *e.g.*  $\text{LiBH}_4$  (ref. 170) and  $\text{Li}_3\text{PS}_4$ .<sup>56</sup> It can further be assumed that the microstructure of the resulting samples affects the measured ionic conductivity and that the strained, nanocrystalline nature of the BM- $\text{Na}_3\text{PS}_4$  is beneficial to macroscopic ion transport.

In conclusion, ball-milling has been shown to have a clearly beneficial effect on the macroscopic ionic conductivity of  $\text{Na}_3\text{PS}_4$ . Although the high-temperature cubic polymorph is stabilized, probably due to the applied stresses during milling, this average structure cannot fully explain the increase in conductivity given that the resulting local structures show the same tetragonal distortions. It is believed that one or a combination of the following is at the origin of the enhanced ion transport:<sup>75</sup> (a)  $\text{Na}^+$  defect introduction, (b) a strained local structure (c) nanocrystalline structure. Overall, the efficacy of mechanochemistry in increasing the conductivity of ion conductors is a promising route for future development and merits further study, and local structural changes must not be ignored and need to be exploited.

### 3.2 Mechanochemically synthesized fluorides: local structures and ion transport

Another class of solid electrolyte from which we can understand the difference between conventional solid-state and mechanochemical routes are fluoride ion conductors. Because of the small size and monovalent nature of  $\text{F}^-$ , these materials have drawn the attention of the battery community.<sup>171,172</sup> A major breakthrough happened when a mechanochemical route was introduced to create nanostructured fluorides benefiting from crystal defects and space charge layer formation at the grain interface. Fluoride ion conductors mostly crystallize in two different structure types: fluorite-type  $\text{MF}_2$  with  $\text{M} = \text{Ca}, \text{Ba}, \text{Sr}, \text{Sn}$  and tsynsite-type  $\text{MF}_3$  with  $\text{M} = \text{La}, \text{Ce}, \text{Pr}, \text{Nd}$ .<sup>124</sup> The binary halide  $\text{SnF}_2$  (monoclinic structure) shows a drastic rise in ionic conductivity from  $4 \times 10^{-3} \text{ mS cm}^{-1}$  to  $0.2 \text{ mS cm}^{-1}$  at  $100^\circ\text{C}$  when ball milled for several hours, which is associated with reduction of crystallites to nanoscale dimensions and resulting microstrain.<sup>173</sup> The ternary layered heterostructured halides,  $\text{MF}_2\text{-SnF}_2$  ( $\text{M} = \text{Pb}, \text{Ba}$ ) show the highest conductivity among the fluoride ion conductors.<sup>174-177</sup>  $\text{PbSnF}_4$  and  $\text{BaSnF}_4$  can be synthesized *via* both high temperature solid-state routes and mechanochemical milling. The mechanochemically-synthesized  $\text{BaSnF}_4$  is considered as one of the fastest conducting fluoride electrolytes, with a room temperature ionic

conductivity of  $0.7 \text{ mS cm}^{-1}$ .<sup>174</sup> The higher ionic conductivity is the result of a small crystallite size ( $\sim 25 \text{ nm}$ ), crystal defects, and large interfacial areas beneficially influencing  $\text{F}^-$  ion diffusion.

As discussed earlier, the mechanochemical synthesis is a well-known route to prepare metastable phases. As an example,  $\text{BaF}_2\text{-CaF}_2$  solid solutions cannot be prepared *via* high temperature solid-state route because of the cationic radius difference ( $\text{Ba}^{2+}$ :  $1.42 \text{ \AA}$ ;  $\text{Ca}^{2+}$ :  $1.12 \text{ \AA}$ ).<sup>178</sup> However, successful synthesis of  $\text{Ba}_x\text{Ca}_{1-x}\text{F}_2$  was reported *via* a high energy ball-milling process, which decomposes upon heat treatment confirming the metastable nature of the solid solution.<sup>179</sup> The ionic conductivity values for  $\text{Ba}_{0.5}\text{Ca}_{0.5}\text{F}_2$  amounts to  $\sim 1.4 \text{ mS cm}^{-1}$  at  $281^\circ\text{C}$ , which is almost two orders of magnitude higher than that of nanocrystalline  $\text{BaF}_2$ . Mixtures of  $\text{BaF}_2$  and  $\text{LaF}_3$  have been extensively studied over the past few years to understand the influence of aliovalent substitution on  $\text{F}^-$  ion transport.<sup>180,181</sup> In contrast to  $\text{BaF}_2\text{-CaF}_2$ , the  $\text{BaF}_2\text{-LaF}_3$  solid solution can be prepared *via* both high temperature solid-state route as well as mechanochemical syntheses routes. The benefit of mechanochemistry, however, is the defect formation which is required to achieve higher conductivities compared to their highly ordered, crystalline counterparts in  $\text{BaF}_2\text{-LaF}_3$ . For instance,  $\text{Ba}_{0.6}\text{La}_{0.4}\text{F}_{2.4}$  shows the highest conductivity of  $0.19 \text{ mS cm}^{-1}$  at  $160^\circ\text{C}$ .<sup>180</sup>

### 3.3 Cooling routines affecting disorder and ionic transport in $\text{Li}_6\text{PS}_5\text{X}$

Lithium argyrodite superionic conductors with high ionic conductivity and mechanically soft nature are promising candidates for commercially viable solid electrolytes.<sup>10,14,23,55,182</sup> A high ionic conductivity that directly correlates with structural disorder raises intense scientific interest in terms of structure-composition-transport relationships.<sup>14,53,183-185</sup> The crystal structure of the halide containing Li-argyrodites  $\text{Li}_6\text{PS}_5\text{X}$  ( $\text{X} = \text{Cl}, \text{Br}, \text{I}$ ) (shown in Fig. 7a) is cubic at room temperature, consisting of  $\text{X}^-$  forming a face-centered cubic sublattice with *ortho*-thiophosphate  $\text{PS}_4^{3-}$  units on the octahedral voids and so-called “free sulfur”,  $\text{S}^{2-}$  not bound to P, in half of the tetrahedral voids.  $\text{Li}^+$  resides on three distinct sites and forms a cage-like structure around the 4d site.<sup>186</sup> A high degree of intrinsic  $\text{X}^-/\text{S}^{2-}$  site-disorder (between this site and 4a, as seen in Fig. 7b) is responsible for fast ion conduction, particularly in  $\text{Li}_6\text{PS}_5\text{Cl}_{1-x}\text{Br}_x$  solid solutions. This disorder is drastically reduced with increasing iodine content in  $\text{Li}_6\text{PS}_5\text{Br}_{1-x}\text{I}_x$ , accompanied by stark reduction in the ionic conductivity (Fig. 7c).<sup>14</sup> As the structure becomes ordered, the activation barriers for ionic motion increases, and with it, the conductivity drastically decreases. The  $\text{X}^-/\text{S}^{2-}$  site-disorder can be re-introduced in the intrinsically ordered  $\text{Li}_6\text{PS}_5\text{I}$  structure through aliovalent substitutions *e.g.*  $\text{Li}_{6+x}\text{P}_{1-x}\text{Ge}_x\text{S}_5\text{I}$ ,  $\text{Li}_{6+x}\text{P}_{1-x}\text{Si}_x\text{S}_5\text{I}$ , and  $\text{Li}_{6+x}\text{Sb}_{1-x}\text{Si}_x\text{S}_5\text{I}$ .<sup>13,32,92</sup> Despite an evident structure-composition-transport relationship, it has been challenging to experimentally deconvolute individual factors influencing ionic transport, *e.g.* lattice polarizability, number of carriers, and structural disorder. To overcome this



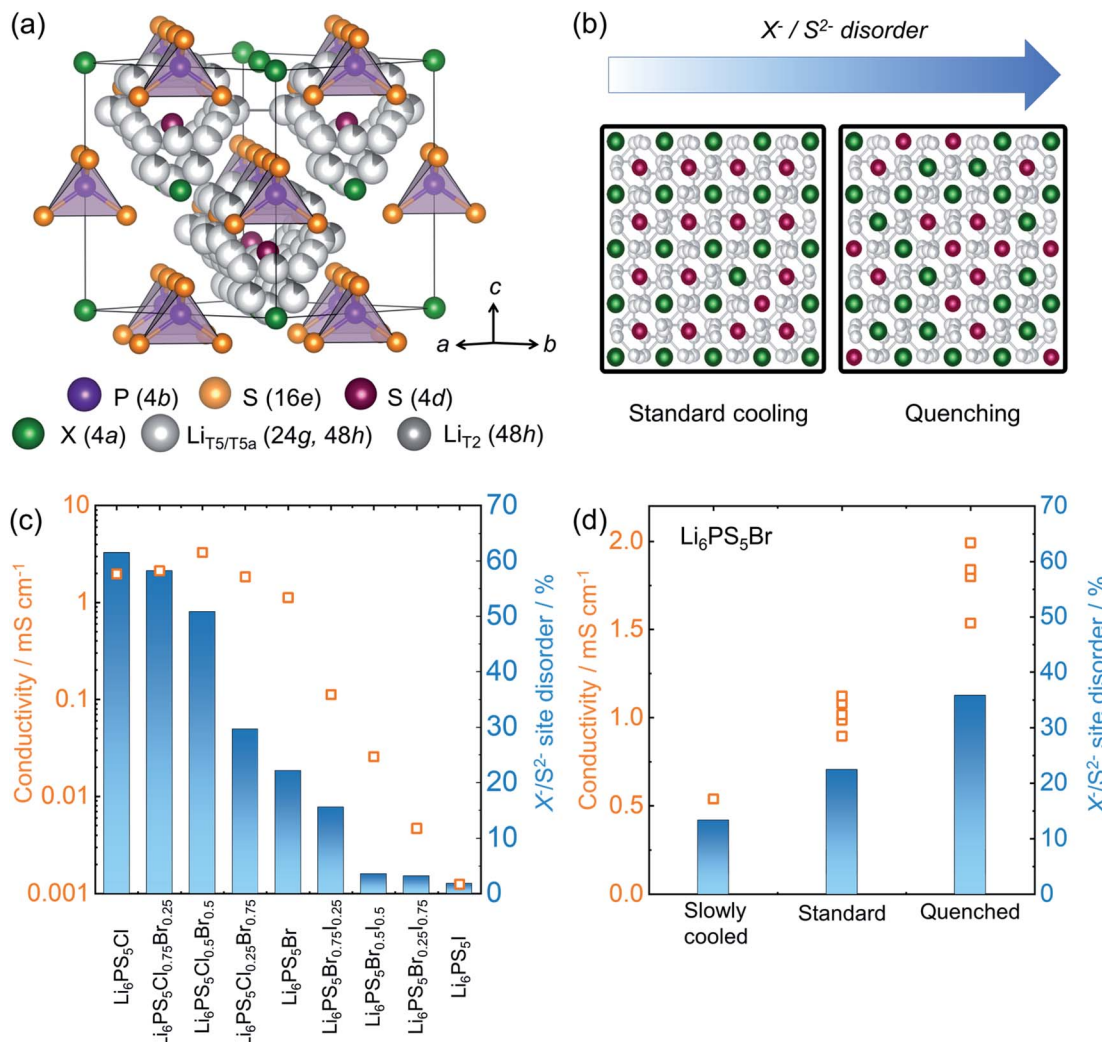


**Fig. 7** Structure of lithium-argyrodites and a structure–transport relationship. (a) A unit cell structure of room temperature lithium argyrodite  $\text{Li}_6\text{PS}_5\text{X}$  ( $\text{X} = \text{Cl}, \text{Br}, \text{I}$ ) phase. (b) The schematic represents lowering of  $\text{Li}^+$  diffusion barrier upon enhanced site-disorder resulting in an enhanced ionic conductivity. (c) A correlation between site-disorder percentage and the resulting conductivity. The more the structure is ordered, the lower the conductivity becomes. (d) The fraction of site disorder  $\text{X}^-/\text{S}^{2-}$  can be kinetically engineered by systematically altering synthesis conditions, corroborating the disorder–transport relationship. Data digitized from ref. 14 and 84.

complication, recent work has varied the reaction kinetics with a systematically modified synthesis conditions, enabling isolation of the impact of the structural disorder.<sup>84</sup>  $\text{Li}_6\text{PS}_5\text{Br}$  was pre-synthesized mechanochemically, followed by heat treatment, with various reaction times (soaking times) and cooling speeds. The variation in the soaking time showed little end effect, revealing rapid reaction kinetics, achieving a crystalline  $\text{Li}_6\text{PS}_5\text{Br}$  within one minute of annealing. However, it was the variation in cooling speed after the reaction that severely impacted the resulting structural disorder and, with it, ionic conductivity, as shown in Fig. 7d. Thermodynamically, entropy stabilizes the disorder formation at elevated temperature. Upon cooling, the amount of those entropically introduced disorders can be kinetically frozen depending upon the rate of cooling compared to the rate at which the disorder is able to relax. As a consequence, a higher disorder can be trapped in the structure by a rapid quenching with liquid

nitrogen. Subsequent work showed that a precise control of the disorder can be made by heating a minimally-disordered, slow-cooled sample to various temperatures followed by quenching, with an achievable range of  $\text{X}^-/\text{S}^{2-}$  disorder of 10–40%.<sup>187</sup>

Clearly synthesis protocols affect the disorder and local structure and with it the ionic transport in solid electrolytes. In case of the lithium argyrodites, the structural disorder, tailorable by a systematic control over the synthesis conditions, play a vital role in transport as it directly affects the  $\text{Li}^+$  distribution and diffusion energy landscape; this could likely be applicable to many other materials as well.

#### 3.4 Milling and crystallization effects in $\text{Li}_3\text{MCl}_6$

The development of halide based solid ionic conductors started in 1930 with lithium halide salts ( $\text{LiX}$ ;  $\text{X} = \text{Cl}, \text{Br}, \text{I}$ ).<sup>188</sup> To improve the conductivity of these materials, substituent metals

have been introduced: divalent<sup>189</sup> (mainly the first row transition metals and Mg, Pb, *etc.*) and trivalent (mainly Group 3 elements Sc, Y; rare earth elements, La–Lu,<sup>69,190–194</sup> Group 13 elements, especially In<sup>29</sup>). Nevertheless, these halide materials were initially characterized as poor ion conductors until 2018 when Asano *et al.* achieved  $\sim 1$  mS cm<sup>-1</sup> in conductivity from  $\text{Li}_3\text{YX}_6$  (X = Cl, Br), by employing mechanical milling.<sup>28</sup> From these materials,  $\text{Li}_3\text{YCl}_6$  (isostructural to  $\text{Li}_3\text{ErCl}_6$ ) crystallizes in a trigonal cell with an hexagonal close packed (hcp) anion sublattice, whereas  $\text{Li}_3\text{YBr}_6$  has a monoclinic structure with cubic closed pack (ccp) anion framework. Both Li and Y occupy the octahedral voids. In  $\text{Li}_3\text{YCl}_6$ , the yttrium can occupy three distinct crystallographic sites (M1 at Wyckoff position 1a and M2, M3 at Wyckoff positions 2d) as shown in Fig. 8a. The edge shared  $\text{LiCl}_6^{5-}$  octahedra forms a honeycomb-like arrangement (Fig. 8b).

Recent work has shown the large influence of synthesis parameters on the crystal structure and resulting ionic transport of these materials.<sup>28</sup> The lower crystallinity of  $\text{Li}_3\text{YCl}_6$  and  $\text{Li}_3\text{YBr}_6$  when synthesized by ball-milling leads to room temperature ionic conductivities of 0.51 mS cm<sup>-1</sup> and 0.72 mS cm<sup>-1</sup>, respectively. A significant difference in the conductivity has been observed when the crystallinity of the ball milled

product was improved through high temperature annealing. Whereas the crystalline  $\text{Li}_3\text{YCl}_6$  has a reduced ionic conductivity of  $\sim 0.03$  mS cm<sup>-1</sup>, the  $\text{Li}_3\text{YBr}_6$  shows superior conductivity of 1.7 mS cm<sup>-1</sup> after the annealing process. The plausible explanation for this contrasting result is the difference in the anion sublattice structures. Schlem *et al.* have recently investigated the influence of the synthesis methods on  $\text{Li}_3\text{MCl}_6$  (M = Er, Y) showing an M2–M3 site disordering, which results in different ionic transport properties.<sup>69</sup>  $\text{Li}_3\text{ErCl}_6$  and  $\text{Li}_3\text{YCl}_6$  were synthesized by high temperature solid-state reaction and mechanochemical synthesis. To understand the impact of crystallization on the structure and ionic conductivity, mechanochemically synthesized samples were subjected to an additional crystallization step, which further tunes M2–M3 site-disorder and thus lithium ion transport. Even though mechanochemical synthesis causes a high M2–M3 site-disorder (up to almost 100%, or a complete site-inversion), the classic high-temperature ampoule syntheses result in only a low degree of disorder as seen in Fig. 8c. The cation site disorder induces a Li-redistribution in the Li-substructure which itself leads to significant change in the structural windows of the Li-ion jump and hence the activation barriers for Li-ion migration as depicted in Fig. 8d. Even in other compositions in these halide

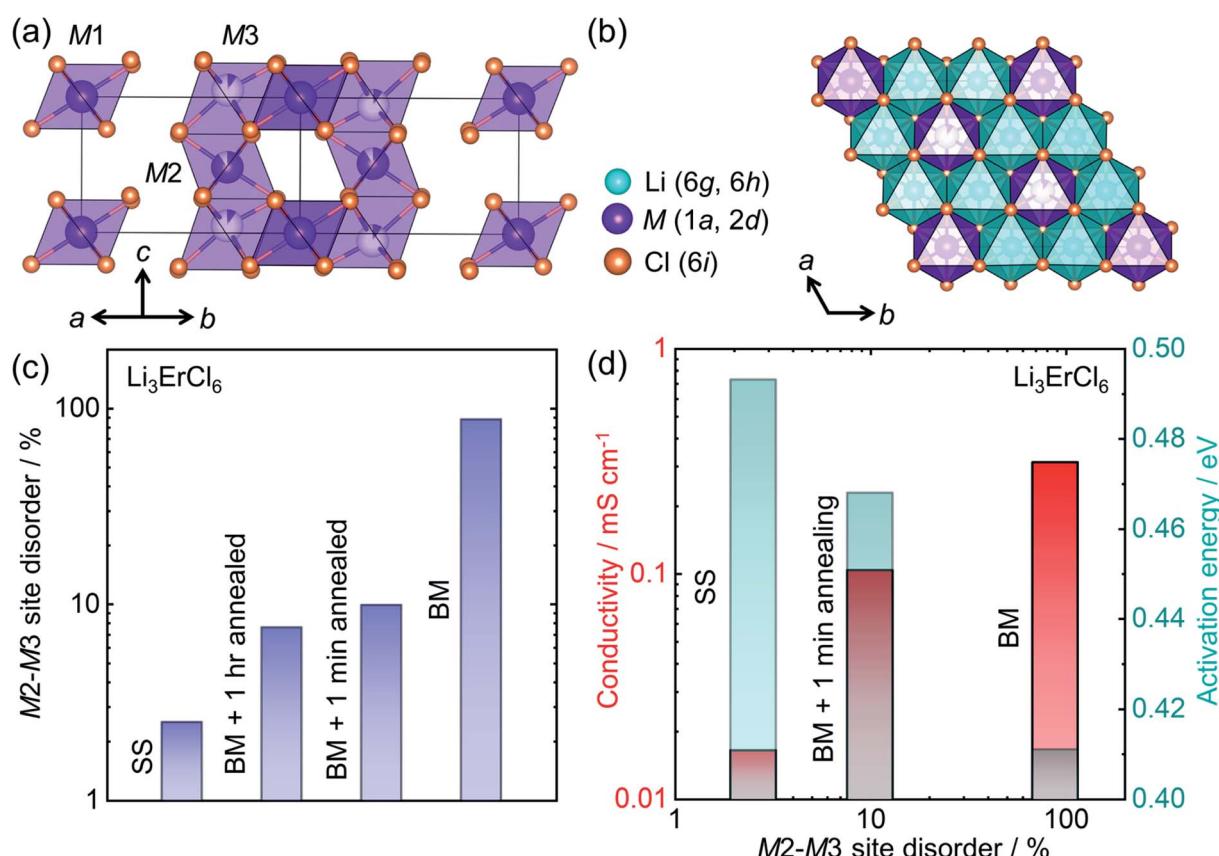


Fig. 8 Structure–transport correlation in  $\text{Li}_3\text{MCl}_6$  (M = Er, Y) (a)  $\text{MCl}_6^{3-}$  octahedra form a trigonal unit cell in  $\text{Li}_3\text{MCl}_6$  where M occupies three different crystallographic sites. (b) Lithium occupies octahedral voids forming edge-shared  $\text{LiCl}_6^{5-}$  octahedra which surround each  $\text{ErCl}_6^{3-}$  octahedron in a honeycomb arrangement in the *a*–*b* plane. (c) Evolution of the M2–M3 site-disorder as a function of synthetic conditions ('solid-state synthesis' corresponding to SS, BM = 'ball milling'). (d) correlation of ionic conductivity and activation energy with M2–M3 site disorder. Data digitized from ref. 69.



conductors, mechanochemical syntheses affect the ionic transport significantly.<sup>28,195,196</sup>

### 3.5 Solvent influence on crystallization, phase formation and ionic conductivity in Li-P-S phases

Most superionic thiophosphates share the predominant structural motif of  $\text{PS}_4^{3-}$  tetrahedra (e.g.  $\text{Li}_3\text{PS}_4$ ,  $\text{Li}_7\text{PS}_6$ ,  $\text{Li}_6\text{PS}_5\text{X}$ ,  $\text{Li}_4\text{PS}_4\text{I}$ ,  $\text{Li}_7\text{P}_3\text{S}_{11}$ , and many amorphous  $\text{Li}_2\text{S}:\text{P}_2\text{S}_5$  compositions). Reports seem to indicate that after the formation of  $\text{PS}_4^{3-}$  units in solution (typically from  $\text{Li}_2\text{S}$  and  $\text{P}_4\text{S}_{10}$  starting materials), solvent molecules strongly complex to form  $\text{Li}_3\text{PS}_4 \cdot n\text{solvent}$ ; the number of solvent molecules per unit varies but is typically 2–3.<sup>56,86,197</sup> The stability of these units seem to be such that, even when additional  $\text{Li}_2\text{S}$  or  $\text{LiX}$  ( $\text{X} = \text{Cl}, \text{Br}, \text{I}$ ) are present, the predominant initial product contains the crystalline solvent complex, and stoichiometric products such as  $\text{Li}_7\text{P}_3\text{S}_{11}$  or  $\text{Li}_6\text{PS}_5\text{X}$  are only achieved after higher-temperature heat treatments in the solid-state.<sup>65</sup> This is to say that the “solution synthesis” aspects of thiophosphates are only part of the story; the specific effects of solvents offer deeper complexity than simply a reaction medium, and what happens after treatment in solution can be just as important to the resulting product.

#### 3.5.1 Effects of heat treatments after solution synthesis.

Heat treatments are often needed to remove residual solvent(s), influence crystallinity, or as part of a chemical reaction to form the final desired phases. As noted, electrolytes produced in solution tend to have solvent molecules intimately complexed. Solvent-complexed  $\text{Li}_3\text{PS}_4 \cdot 2\text{ACN}$ , for example, retains minimal  $\text{Li}^+$  conductivity ( $10^{-6} \text{ mS cm}^{-1}$  at room temperature); this increases to  $0.1 \text{ mS cm}^{-1}$  after ACN removal at  $200^\circ\text{C}$ .<sup>198</sup> Complexed THF can be removed at lower temperatures ( $\sim 80^\circ\text{C}$ ), bringing the conductivity to  $10^{-2} \text{ mS cm}^{-1}$ ; the conductivity rises to  $0.1 \text{ mS cm}^{-1}$  up to  $140^\circ\text{C}$  and then mildly fades at higher temperatures, so clearly further processes are occurring.<sup>199</sup> Synthesis in ethyl acetate resulted in a crystalline solvent complex; removal of ethyl acetate ( $\sim 88^\circ\text{C}$ ) first resulted in an amorphous material, followed by crystalline  $\text{Li}_3\text{PS}_4$  after  $160^\circ\text{C}$ .<sup>197</sup> In that work, the heat treatment from  $110^\circ\text{C}$  to  $160^\circ\text{C}$  resulted in conductivity increasing from  $10^{-2}$  to  $0.1 \text{ mS cm}^{-1}$ . From these examples it can be expected that every solvent used to synthesize  $\text{Li}_3\text{PS}_4$  may have different requirements for removal and optimization of conductivity by heat treatment. This is especially important due to the central nature of  $\text{Li}_3\text{PS}_4$  in many synthetic pathways of thiophosphate conductors.<sup>65</sup>

For the synthesis in acetonitrile of  $\text{Li}_7\text{P}_3\text{S}_{11}$ , composed of both  $\text{PS}_4^{3-}$  and  $\text{P}_2\text{S}_7^{4-}$  units, it is clear that in solution processes, only the highly stable  $\text{PS}_4^{3-}$  units form; the additional  $\text{P}_2\text{S}_7^{4-}$  units are only formed at elevated temperatures of  $200\text{--}260^\circ\text{C}$ .<sup>200</sup> Higher temperatures decompose the  $\text{Li}_7\text{P}_3\text{S}_{11}$ .<sup>201</sup> As  $\text{Li}_3\text{PS}_4$  was determined to be an important intermediate in the overall synthesis from  $\text{Li}_2\text{S}$  and  $\text{P}_4\text{S}_{10}$ ,<sup>200</sup> careful scrutiny of the solvent chemistry with this compound, and what effects arise as solvent molecules leave at higher temperatures, may be of high importance in the synthesis of  $\text{Li}_7\text{P}_3\text{S}_{11}$ .

In the case of argyrodites  $\text{Li}_6\text{PS}_5\text{X}$  (using the higher-conducting phases with  $\text{X} = \text{Br}, \text{Cl}$ , as examples), either by

synthesis or dissolution in ethanol, crystalline argyrodite (rather than a crystalline or amorphous *solvato* complex, as evidenced by X-ray diffraction) can be recovered by removal of solvent at as little as  $80^\circ\text{C}$ ; however, the conductivity remains low, even in the range of  $10^{-2} \text{ mS cm}^{-1}$ .<sup>202</sup> Heat treatment up to  $150\text{--}200^\circ\text{C}$  improves the conductivity to  $0.1 \text{ mS cm}^{-1}$ , but ultimately heating to  $550^\circ\text{C}$  fully recovers conductivity to the expected  $\text{mS cm}^{-1}$  range.<sup>135</sup> So far, these high heat treatments are needed, which partially alleviates the beneficial approach of solution synthesis in argyrodites, and future work for low temperature syntheses is needed. A generalized schematic representing the influence of processing temperature on phase formation, its stability and ionic conductivity is shown in Fig. 9a.

**3.5.2 Morphology control by solvent.** Solvent systems appear to offer a facile way to control the morphology of  $\text{Li}_3\text{PS}_4$  particles. When prepared from  $\text{Li}_2\text{S}$  and  $\text{P}_4\text{S}_{10}$ , solvent molecules complex with the resulting  $\text{PS}_4^{3-}$  units. Upon crystallization, two well-defined morphologies have been demonstrated: block-shaped crystals of  $\text{Li}_3\text{PS}_4 \cdot 3\text{THF}$ , and plate-shaped  $\text{Li}_3\text{PS}_4 \cdot 2\text{ACN}$ . It was even found that the  $\text{Li}_3\text{PS}_4 \cdot 3\text{THF}$  crystals could convert to plate-shaped  $\text{Li}_3\text{PS}_4 \cdot 2\text{ACN}$  upon immersion in acetonitrile (Fig. 9b).<sup>86</sup> Removal of the residual solvent molecules at elevated temperature seems to result in the preservation of the overall crystal morphology, therefore offering a detailed level of control over the shape of prepared electrolyte particles. Importantly, it was found that both morphologies, after conversion to  $\beta\text{-Li}_3\text{PS}_4$ , achieved approximately the same conductivity ( $0.1 \text{ mS cm}^{-1}$ ).<sup>58</sup> These explorations into plate-like morphologies discussed the possibility of creating solid electrolyte films, but the varied structures open the door for carefully exploring the effect of solid electrolyte morphology on the more complicated systems of a full cell. Besides the effect of THF and acetonitrile, other solvents such as dimethyl carbonate (combined with mechanical shaking) led to indeterminate morphology.<sup>61</sup>

**3.5.3 Consequences of solvent selection with multi-step reactions.** It has already been discussed above that some electrolytes prove difficult to synthesize in a single solvent and may be better produced in multiple solvents stepwise (or simultaneously in the case of  $\text{Li}_3\text{PS}_4$  in NMF/hexane<sup>57</sup>). It was also shown that some compositions such as  $\text{Li}_7\text{P}_3\text{S}_{11}$  may not be accessible by solvent synthesis alone, instead requiring heat treatment not just to increase conductivity but to form the required structural polyhedra. Xu *et al.* synthesized  $\text{Li}_7\text{P}_3\text{S}_{11}$  by reacting  $\text{Li}_2\text{S}$  with  $\text{P}_2\text{S}_5$  in THF, acetonitrile, and a mixture of both.<sup>203</sup> They found that acetonitrile gave the best result of primarily  $\text{Li}_7\text{P}_3\text{S}_{11}$ , THF resulted in mostly low-conducting  $\text{Li}_4\text{P}_2\text{S}_6$ , and a mixture of both solvents gave  $\text{Li}_7\text{P}_3\text{S}_{11}$  with impurities of  $\text{Li}_4\text{P}_2\text{S}_6$ . THF and acetonitrile were both demonstrated above to each produce equally well-conducting  $\text{Li}_3\text{PS}_4$  at the proper stoichiometry, and it was shown that  $\text{Li}_7\text{P}_3\text{S}_{11}$  requires a heat treatment step; the seemingly negative influence of THF in the overall synthesis of  $\text{Li}_7\text{P}_3\text{S}_{11}$  could very well be due to morphology or heterogeneity of intermediates in the lead-up to higher temperature reaction, possibly due to induced local deviations of stoichiometry. This is interesting with this



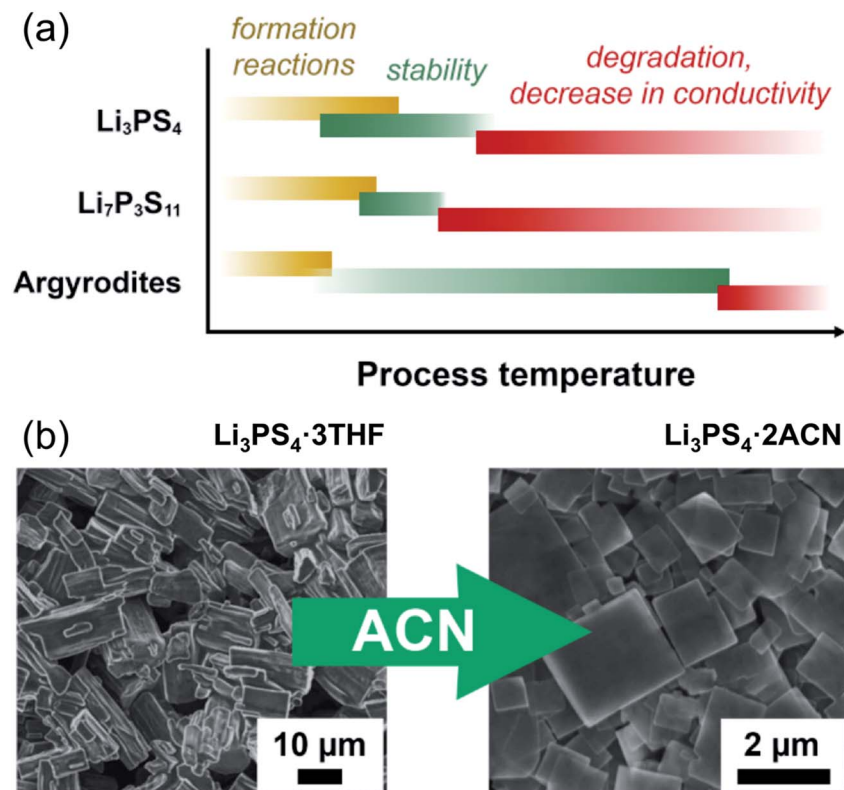


Fig. 9 (a) A simplification showing the effect of temperature throughout processing of three types of lithium thiophosphates.  $\text{Li}_3\text{PS}_4$ , due to the diversity of solvents used to produce it, shows a wide span of temperatures over which the material forms and solvent is removed (roughly 60 to 200 °C); it is stable, with some decrease in conductivity, until at higher temperatures the phase changes.  $\text{Li}_7\text{P}_3\text{S}_{11}$  does not form until a higher temperature solid-state reaction (above 200 °C) occurs, but decomposes to  $\text{Li}_4\text{P}_2\text{S}_6$  above roughly 300 °C. For the argyrodites, the formation is generally complete after solvent removal below 100 °C. The conductivity gradually increases with heat treatment. (b) An example of morphological change with the same composition (adapted from ref. 198).  $\text{Li}_3\text{PS}_4$  produced with THF shows block-like crystals of  $\text{Li}_3\text{PS}_4 \cdot 3\text{THF}$ ; after stirring in acetonitrile, the composition changes to  $\text{Li}_3\text{PS}_4 \cdot 2\text{ACN}$ , and the morphology changes to flat plate-like squares. This figure is adopted with permission from ref. 198. Copyright 2018 John Wiley and Sons.

reaction, given that THF is generally reported as a faster solvent in which to make  $\text{Li}_3\text{PS}_4$ . The argyrodites offer the starker depiction of this; they generally seem not to be accessible from  $\text{Li}_2\text{S}$ ,  $\text{P}_4\text{S}_{10}$ , and lithium halide salts directly in solvent reaction; either  $\text{Li}_3\text{PS}_4$  is preferentially produced in a solvent like THF, or the materials show side reactions in a solvent like ethanol, so the process is split into two steps with distinct solvents.<sup>135</sup> It may be the case that the steps of the reaction simply are not compatible with a single solvent, but if the underlying stabilities, mechanisms, and kinetics are better understood, it might also be possible to engineer a solvent-mixture solution to the problem.

Through these case studies, producing  $\text{PS}_4^{3-}$  units from precursors in solution seems at this point fairly straightforward. However, though this is a dominant structural moiety in thiophosphate superionic conductors, the solution-based synthesis (and post-synthetic processing) of more complex compositions and structures requires much deeper attention. To properly synthesize desired compounds may require multiple solvents, either mixed or selected at various stages, as well as carefully controlled heat treatments. In the selection of solvents, undesired reactivity of solvent with precursors and products must be monitored and mitigated.

### 3.6 Synthesis of high performing metastable phases – $\text{Li}_{10}\text{Ge}_2\text{S}_{12}$ and $\text{Na}_{10}\text{Sn}_2\text{PS}_{12}$

Quaternary chalcogenides are some of the best performing solid electrolytes in terms of ionic conductivity.<sup>11,15,25</sup> The discovery of  $\text{Li}_{10}\text{Ge}_2\text{PS}_{12}$ , which first demonstrated solid-state lithium ionic conductivity as fast as in liquids, jumpstarted the development of room temperature lithium solid-state batteries.<sup>15</sup> Most of such known quaternary phases can be considered as mixtures of (usually lower ion-conducting) ternary phases. Their structures are based on the arrangement of isolated  $\text{MCh}_4$  ( $\text{M} = \text{P}$ ,  $\text{Sb}$ ,  $\text{Si}$ ,  $\text{Ge}$ ,  $\text{Sn}$ ;  $\text{Ch} = \text{S}$ ,  $\text{Se}$ ) tetrahedra coordinating  $\text{Li}^+$  (in mixed tetrahedral and octahedral sites) or  $\text{Na}^+$  (in mainly octahedral sites) to form diffusion pathways. The sodium compositional analogues follow a distinct structural motif exemplified in the  $\text{Na}_{11}\text{Sn}_2\text{S}_{12}$  archetype.<sup>204–206</sup> Due to their quaternary nature, these phases exist in phase equilibrium with multiple ternary and binary compounds which complicates their synthesis. This case study aims to discuss the challenges and opportunities relating to the synthesis of these high-performance compounds.

*Ab initio* calculations have played a key role in understanding the behavior of ternary chalcogenides, since their discovery.<sup>207–209</sup> The  $\text{Li}_{10}\text{Ge}_2\text{PS}_{12}$  compounds are enthalpically unstable against decomposition at 0 K. Consequently, their



successful synthesis hinges on entropic stabilizing effects at finite temperature that favor mixing of the  $\text{MCh}_4$  tetrahedra and disorder of mobile cations as well as single-phase formation. For example,  $\text{Li}_{10}\text{Ge}_2\text{PS}_{12}$  (LGPS) is enthalpically less stable than a 2 : 1 mixture of  $\text{Li}_4\text{GeS}_4$  and  $\text{Li}_3\text{PS}_4$ ,<sup>207</sup> which can thus appear as synthesis side-products under non-optimized conditions, with negative consequences on the ion transport properties of the resulting material. For  $\text{Na}_{11}\text{SnP}_2\text{S}_{12}$ -type compounds, comparably smaller decomposition energies towards ternary products or even thermodynamic stability at 0 K is reported. Here, the stability of compounds with different immobile cationic ratios  $\text{M}'\text{:M}''$  ( $\text{M}' = \text{P, Sb}$ ;  $\text{M}'' = \text{Sn}$ ) are currently subject to investigation.<sup>210</sup> Nevertheless, it seems that a lot of these quaternary materials are metastable and rely on specific synthesis conditions such as ball-milling, or control of synthesis according to the phase diagram.

Arguably the most important, but hitherto underused, tool in optimizing the synthesis of such ternary phases is a phase diagram describing phase equilibria at finite temperatures. Such phase diagrams are practically only accessible experimentally due to the difficulties of *ab initio* calculation methodologies to accurately capture the effects of temperature.<sup>211</sup> As discussed in the solid-state synthesis section (Section 2.1), high temperature tends to favor single-phase behavior, which is key in synthesizing pure quaternary phases. Still, excessive heating can also lead to (partial and/or incongruent) melting, which is counterproductive. A successful phase diagram identifies the temperature and composition ranges of single-phase domain(s) and characterizes the melting behavior of the system, allowing for the rational tailoring of the synthesis parameters to the desired product.

Fig. 10a shows the  $\text{Li}_4\text{GeS}_4\text{--Li}_3\text{PS}_4$  quasi-binary phase diagram containing  $\text{Li}_{10}\text{Ge}_2\text{PS}_{12}$  constructed by Hori *et al.*<sup>102</sup> Five unique solid phases are accessible in this composition-temperature space:  $\text{Li}_4\text{GeS}_4$  ( $\beta'$ ) in the germanium-rich end;  $\alpha$ ,  $\beta$ , and  $\gamma\text{-Li}_3\text{PS}_4$  in the phosphorus-rich end; and the highly ion conductive  $\text{Li}_{10}\text{Ge}_2\text{PS}_{12}$  in between. It is evident from the phase diagram that a  $\text{Li}_{10}\text{Ge}_2\text{PS}_{12}$  composition will start partially melting at  $\sim 550$  °C into a phosphorus-rich melt which would crystallize as  $\text{Li}_3\text{PS}_4$  upon subsequent cooling. Further heating will cause a phase transition of the remaining  $\text{Li}_{10}\text{Ge}_2\text{PS}_{12}$  phase to  $\text{Li}_4\text{GeS}_4$ , which would persist after cooling.<sup>212</sup> Altogether, this phase diagram suggests that the material should be synthesized at around 500 °C, which is the maximum temperature possible while avoiding incongruent melting and crystallization of the ternaries; and indeed, the temperature range 500–550 °C is utilized in most reports (Fig. 10b).

In addition, there exists a compositional window of approximately  $0.5 < x < 0.67$  at room temperature ( $0.45 < x < 0.67$  at 500 °C) of phase stability for an  $\text{Li}_{10}\text{Ge}_2\text{PS}_{12}$ -type phase. In other words, an LGPS-type structure can crystallize in compositions richer in Ge than the nominal  $\text{Li}_{10}\text{GeP}_2\text{S}_{12}$ , up to approximately  $\text{Li}_{10.5}\text{Ge}_{1.5}\text{P}_{1.5}\text{S}_{12}$ .<sup>213</sup> In contrast, any excess of phosphorus beyond the nominal composition would cause crystallization of  $\text{Li}_3\text{PS}_4$ . As such, if a single  $\text{Li}_{10}\text{Ge}_2\text{PS}_{12}$  phase is intended, a slightly Ge-rich composition should be targeted to account for experimental error in the weighing of reagents. In fact, the Ge-rich composition of the archetypical  $\text{Li}_{10}\text{Ge}_2\text{PS}_{12}$  stoichiometry shows increased ionic conductivity.<sup>213</sup>

Overall, knowledge of relevant phase diagrams has enabled the synthesis of pure phases and single crystals<sup>103</sup> to build on the fundamental understanding of  $\text{Li}_{10}\text{Ge}_2\text{PS}_{12}$ . Furthermore, the phase diagram can allow for the synthesis of phase mixtures

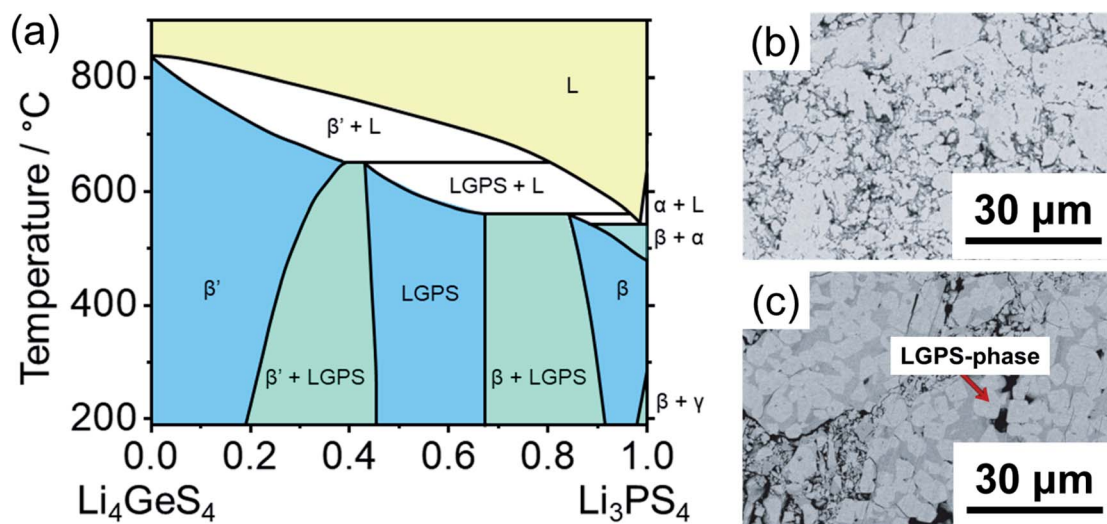


Fig. 10 (a)  $\text{Li}_4\text{GeS}_4\text{--Li}_3\text{PS}_4$  quasi-binary phase diagram proposed by Hori *et al.*<sup>102</sup> As suggested by the phase diagram, variation of synthesis temperature and cooling controls on the phase formation and microstructures. Scanning electron micrographs (SEM) for the composition  $[(1-x)\text{Li}_4\text{GeS}_4 + x\text{Li}_3\text{PS}_4]$  with  $x = 0.65$  cooled under different condition: slowly cooled synthesis from 550 °C (b) and quenched from 650 °C (c). Uniform contrast in the roughout matrix indicates formation of pure LGPS (b); sample quenched from 650 °C shows rectangular brighter crystalline area surrounded by darker areas corresponding to LGPS-type and  $\text{Li}_3\text{PS}_4$ -rich solid phases, respectively (c). The phase diagram is digitized from ref. 102. SEM images were adopted from ref. 102 with permission. Copyright 2015 John Wiley and Sons.



with controlled microstructures. For example,  $\text{Li}_{10}\text{Ge}_2\text{PS}_{12}$  crystals in an amorphous LPS matrix can be produced by quenching (Fig. 10c) which could alleviate so called “grain-boundary” resistances of such quaternary compounds.<sup>102</sup> Others have examined the crystallization of  $\text{Li}_{10}\text{GeP}_2\text{S}_{12}$  starting from mechanochemically prepared amorphous precursors.<sup>214,215</sup> It was shown that annealing these precursors at moderate temperatures ( $260\text{ }^\circ\text{C} < T < 410\text{ }^\circ\text{C}$ ) resulted in crystallization of the two end-member phases  $\text{Li}_4\text{GeS}_4$  and  $\text{Li}_3\text{PS}_4$ , indicating a kinetic barrier to forming the single  $\text{Li}_{10}\text{Ge}_2\text{PS}_{12}$  phase, even in temperatures where according to the phase diagram of Fig. 10a it should be thermodynamically favored.<sup>214</sup> This can be understood by the need for mobility of the  $\text{PS}_4^{3-}$  and  $\text{GeS}_4^{3-}$  moieties which are statistically mixed in the  $\text{Li}_{10}\text{Ge}_2\text{PS}_{12}$  phase. In this study, temperatures  $450\text{ }^\circ\text{C} < T < 550\text{ }^\circ\text{C}$  were required to crystallize  $\text{Li}_{10}\text{GeP}_2\text{S}_{12}$  and such increase the ionic conductivity of the resulting powder.

From a local structure point of view, the building blocks of (a) the amorphous precursor, (b) a two-phase mixture of  $\text{Li}_4\text{GeS}_4$  and  $\text{Li}_3\text{PS}_4$ , and (c) single-phase  $\text{Li}_{10}\text{GeP}_2\text{S}_{12}$ , are always the same:  $\text{Li}^+$ ,  $\text{GeS}_4^{4-}$  and  $\text{PS}_4^{3-}$ ; the arrangement in the quaternary  $\text{Li}_{10}\text{GeP}_2\text{S}_{12}$  phase yields the most facile local pathways for  $\text{Li}^+$ -ion transport and maximizes ionic conductivity. It is noteworthy that even after the heat treatment, no full crystallization is obtained, giving rise to the possibility to create such  $\text{Li}_{10}\text{GeP}_2\text{S}_{12}$  precipitates in a glassy matrix as by the quenching approach. Similarly in related compounds such as  $\text{Li}_3\text{SiPS}_8$  the synthesis conditions strongly affect the phase formation of lower and faster conducting polymorphs alongside an amorphous side phase limiting the ionic transport.<sup>81</sup>

In  $\text{Na}_{11}\text{SnP}_2\text{S}_{12}$  such a detailed phase diagram and/or the effect of mechanochemical synthesis on structure and transport have yet to be explored. However, the phase width (and thereby a similar two-phase region) of  $\text{Na}_{11}\text{SnP}_2\text{S}_{12} + \text{Na}_3\text{PS}_4$  (analogous to  $\text{Li}_{10}\text{GeP}_2\text{S}_{12} + \text{Li}_3\text{PS}_4$ ) has been investigated in mixtures of  $\text{Na}_4\text{SnS}_4$  and  $\text{Na}_3\text{PS}_4$  yielding the pure  $\text{Na}_{11}\text{Sn}_2\text{PS}_{12}$  structure at a 2 : 1 ratio. Additionally,  $\text{Na}_{11}\text{SnP}_2\text{S}_{12}$ -isostructural  $\text{Na}_{12-x}(\text{Sn}_2\text{Si})_{1-x}\text{P}_x\text{S}_{12}$  and  $\text{Na}_{11}\text{Sn}_2\text{PSe}_{12}$  have been produced by mechanochemical synthesis routes,<sup>216</sup> indicating the likelihood to synthesize  $\text{Na}_{11}\text{SnP}_2\text{S}_{12}$  in a related way. In the Na-quaternary phases grain boundary contributions to the total impedance are often observed making the above-mentioned possibilities worthwhile to explore in the Na based system.<sup>204,217</sup>

### 3.7 Solid-state vs. solution synthesis for $\text{Li-La}_2\text{Zr}_3\text{O}_{12}$ and $\text{Li}_{1+x}\text{Al}_x\text{Ge}_{2-x}(\text{PO}_4)_3$

Garnets ( $\text{Li}_x\text{A}_2\text{B}_3\text{O}_{12}$ )<sup>21,218-220</sup> and Li-NASICONs ( $\text{LiM}_2(\text{PO}_4)_3$ )<sup>105</sup> are typical representatives of solid ion conductors. The conventional synthesis route follows solid-state reaction of the oxide precursors, which usually require high temperatures ( $900\text{--}1230\text{ }^\circ\text{C}$ ), and long dwelling times ( $>12\text{ h}$ ). Furthermore, high-temperature annealing is the additional necessary step to achieve maximum densification to reduce grain boundary resistance. This produces highly crystalline materials with large grain size and low grain boundary density, resulting in a high density and good ionic conductivity. However, lithium loss and

secondary phase formation are two detrimental effects associated with high temperature heat treatment, both of which have a negative impact on the Li-ion conductivity.<sup>21,105</sup> Thus, optimization of the heat treatment parameters such as synthesis temperature and time has become crucial for viable application of these material classes. In addition to the optimization of known synthesis processes, alternative synthesis approaches have been adopted in order to achieve a more cost-effective production. This includes sol-gel methods, thin film processing techniques (radio-frequency magnetron sputtering, pulsed laser deposition, metal-organic chemical vapor deposition and sol-gel spin coating), spray pyrolysis and electrospinning techniques.<sup>21,105,221</sup> In the following section we compare ionic transport properties of  $\text{Li-La}_2\text{Zr}_3\text{O}_{12}$  and  $\text{Li}_{1+x}\text{Al}_x\text{Ge}_{2-x}(\text{PO}_4)_3$  synthesized via solid-state and sol-gel routes.

**3.7.1 Solid-state vs. sol-gel synthesis for  $\text{Li-La}_2\text{Zr}_3\text{O}_{12}$ .** The Li-ion conducting  $\text{Li}_7\text{La}_3\text{Zr}_2\text{O}_{12}$  crystallizes in two stable polymorphs depending upon the synthesis temperature: high temperature synthesis results in a cubic phase which exhibits a disordered lithium-ion distribution.<sup>218</sup> This cubic phase transforms into the tetragonal polymorph having an ordered arrangement of the lithium ions when the synthesis temperature drops down to  $900\text{ }^\circ\text{C}$ .<sup>222</sup> The tetragonal phase exhibits a conductivity two orders of magnitude lower than that of the cubic form due to the filling and ordering of the  $\text{Li}^+$  sites. Murugan *et al.* reported the successful preparation of the high temperature cubic  $\text{Li}_7\text{La}_3\text{Zr}_2\text{O}_{12}$  phase with high  $\text{Li}^+$  conductivity of  $\sim 0.3\text{ mS cm}^{-1}$  from solid-state synthesis,<sup>37</sup> which was later shown to only be stable due to  $\text{Al}^{3+}$  contamination from the crucibles.<sup>223</sup> The conventional synthesis route follows a solid-state reaction of the oxide precursors ( $\text{LiOH}$ ,  $\text{La}_2\text{O}_3/\text{La}_2\text{CO}_3$  and  $\text{ZrO}_2$ ), which usually require continuous mixing *via* solvent-assisted ball milling and prolonged high temperature ( $900\text{--}1230\text{ }^\circ\text{C}$ ) sintering, creating uncontrolled Li-vacancies. The composition and microstructure of the pellets has significant impact on the ionic conductivity, relative density and air stability of the lithium garnets.<sup>100</sup> The grain-boundaries regions are the high energy interface which initiate the reactions between  $\text{Li}_7\text{La}_3\text{Zr}_2\text{O}_{12}$  and moisture, hence reducing the total conductivity after one week of air exposure.<sup>224</sup> To prepare dense pellets and minimize the grain boundary resistance, an additional high temperature sintering ( $\sim 1230\text{ }^\circ\text{C}$ ) step is necessary.<sup>225</sup> Although it results in a highly crystalline structure, large grains with fewer grain boundary, and high density, non-conducting  $\text{La}_2\text{Zr}_2\text{O}_7$  second phase formation results in unavoidable  $\text{Li}^+$ -ion conductivity reduction.<sup>104</sup> To reduce the synthesis temperature, sol-gel routes were developed in which the starting materials are mixed at a molecular level. This approach has received interest due to its several advantages, including the requirement of relatively low sintering temperature, which can result in stoichiometric controllability in the as-synthesized  $\text{Li}_7\text{La}_3\text{Zr}_2\text{O}_{12}$ .  $\text{Li}_7\text{La}_3\text{Zr}_2\text{O}_{12}$  synthesized *via* sol-gel routes requires lower sintering temperature as seen in Fig. 11a. Shimonishi *et al.* has reported the ionic transport properties of cubic and tetragonal  $\text{Li}_7\text{La}_3\text{Zr}_2\text{O}_{12}$  synthesized by sol-gel synthesis using citric acid and ethylene glycol from  $\text{LiNO}_3$ ,  $\text{La}(\text{NO}_3)_3 \cdot 6\text{H}_2\text{O}$ , and  $\text{ZrO}(\text{NO}_3)_2\text{H}_2\text{O}$ , where sintering



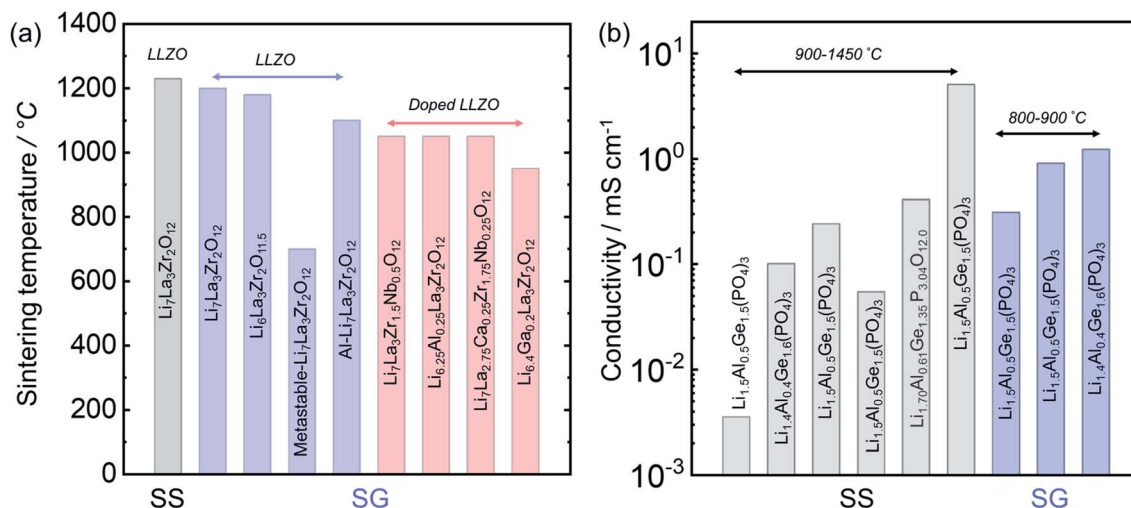


Fig. 11 Influence of synthesis route on the sintering temperature and conductivity of cubic  $\text{Li}_7\text{La}_2\text{Zr}_3\text{O}_{12}$  and  $\text{Li}_{1+x}\text{Al}_x\text{Ge}_{2-x}(\text{PO}_4)_3$ . (a) The sintering temperature for sol-gel (SG) route<sup>41,140,219,226</sup> is lower than solid-state (SS) synthesis,<sup>37</sup> which further decreases with substitution.<sup>224–227</sup> (b) Ionic conductivities of  $\text{Li}_{1+x}\text{Al}_x\text{Ge}_{2-x}(\text{PO}_4)_3$  synthesized via SS<sup>139,231–234</sup> and SG methods.<sup>45,49,235</sup>

temperature was reduced to 1180 °C and 800 °C, respectively.<sup>226</sup> Elemental analysis suggested that the chemical formulas of the cubic and tetragonal phases were  $\text{Li}_6\text{La}_3\text{Zr}_2\text{O}_{11.5}$  and  $\text{Li}_7\text{La}_3\text{Zr}_2\text{O}_{12}$ , respectively. The lower Li-content of the cubic structure is in good agreement with the important role of Li- vacancies to tune the crystal structure and conductivity.<sup>227</sup> Janani *et al.* were able to decrease the sintering temperature for the cubic garnet further to 700 °C by using citric acid as organic complexing agent and butan-1-ol or propan-2-ol as surface active agent.<sup>140</sup> Kokal *et al.* reported the preparation of Al-free nanostructured  $\text{Li}_7\text{La}_3\text{Zr}_2\text{O}_{12}$  (300–500 nm) in the cubic phase at 700 °C by the modified sol-gel Pechini method; it subsequently transforms to the tetragonal phase above 724 °C.<sup>39</sup> Similarly, use of acetate salt as the metal precursor in acetic acid gives rise to formation of metastable cubic  $\text{Li}_7\text{La}_3\text{Zr}_2\text{O}_{12}$  at 750 °C, which further decomposes to  $\text{La}_2\text{Zr}_2\text{O}_7$  above 800 °C.<sup>228</sup>

Room temperature ionic conductivity of sol-gel and solid-state synthesized  $\text{Li}_7\text{La}_3\text{Zr}_2\text{O}_{12}$  is comparable to values reported previously, which further shows possible improvements of a sol-gel route over a solid-state one.<sup>226</sup> Although sol-gel syntheses can offer lower sintering temperatures, they do not improve the atmospheric stability of  $\text{Li}_7\text{La}_3\text{Zr}_2\text{O}_{12}$ .<sup>226,229</sup> Further, the reduction of grain boundary resistance still remains as an open challenge for this material class. Studies on the Li-site disorder are also rare; these could pave the way to achieving higher conducting  $\text{Li}_7\text{La}_3\text{Zr}_2\text{O}_{12}$  derivatives.<sup>229,230</sup>

Despite these challenges and the promising possibility of different synthetic techniques, in-depth studies on how the synthesis conditions can further increase disorder and affect conductivities and even the microstructure and grain boundaries are lacking so far.

**3.7.2 Solid-state vs. solution process for  $\text{Li}_{1+x}\text{Al}_x\text{Ge}_{2-x}(\text{PO}_4)_3$ .** NASICON, the Na-superionic conductor refers to the family of ion conductors which adopt the crystal structure of  $\text{NaZr}_2(\text{PO}_4)_3$ .<sup>20,105</sup> The representative general

formula for these materials is  $\text{AM}_2(\text{PO}_4)_3$ , where A corresponds to the alkali metal ions, Li, Na, or K, and M is usually a tetravalent element like Ge, Zr, or Ti. It consists of distorted hexagonal close packed oxide framework with  $\text{LiO}_6$  units in trigonal antiprismatic coordination, with  $\text{MO}_6$  octahedra and  $\text{PO}_4$  tetrahedra forming a rhombohedral structure at room temperature.

One of the most well-known ionic conductors from this family is  $\text{Li}_{1+x}\text{Al}_x\text{Ge}_{2-x}(\text{PO}_4)_3$ , where substitution of tetravalent  $\text{Ge}^{4+}$  ions by trivalent  $\text{Al}^{3+}$  leads to incorporation of additional  $\text{Li}^+$  in the structure, resulting in higher conductivity. High temperature melt-quenching and sol-gel processes are the common synthesis routes to prepare these materials.<sup>44</sup> Because of the very high synthesis temperature ( $\sim 1500$  °C), lithium loss by vaporization is a common problem associated with the melt quenching reaction. On the contrary, sol-gel methods offer syntheses of phase pure  $\text{Li}_{1+x}\text{Al}_x\text{Ge}_{2-x}(\text{PO}_4)_3$  at much lower temperatures, without Li-loss (Fig. 11b).<sup>45,236</sup> Weiss *et al.* recently reported a simple one-pot solution-phase synthesis of  $\text{Li}_{1+x}\text{Al}_x\text{Ge}_{2-x}(\text{PO}_4)_3$  using  $\text{GeO}_2$  as the replacement of expensive precursor  $\text{Ge}(\text{OC}_2\text{H}_5)_4$ .<sup>50</sup>

The properties of  $\text{Li}_{1+x}\text{Al}_x\text{Ge}_{2-x}(\text{PO}_4)_3$  are highly dependent on the purity of the phase and the Al incorporation into the structure, which often deviates based on synthetic inputs specially different sintering conditions. Hence, optimization of the sintering temperature is key to achieving desirable phases and hence optimized properties. It has been observed that sol-gel synthesis can produce phase pure  $\text{Li}_{1+x}\text{Al}_x\text{Ge}_{2-x}(\text{PO}_4)_3$  up to  $x = 0.5$ , which was not the case for solid-state reactions.<sup>236</sup> The highest total conductivity of  $1.22 \text{ mS cm}^{-1}$  at 25 °C was observed for the sample  $\text{Li}_{1+x}\text{Al}_x\text{Ge}_{2-x}(\text{PO}_4)_3$  with  $x = 0.4$ , which was higher than that of the  $\text{Li}_{1+x}\text{Al}_x\text{Ge}_{2-x}(\text{PO}_4)_3$  ( $x = 0.5$ ) glass-ceramic reported by Xu *et al.* ( $0.725 \text{ mS cm}^{-1}$ ), and those of the  $\text{Li}_{1+x}\text{Al}_x\text{Ge}_{2-x}(\text{PO}_4)_3$  ( $x = 0.5$ ) prepared using a solid-state reaction precursor ( $0.0035 \text{ mS cm}^{-1}$ ). *In situ* synchrotron X-ray

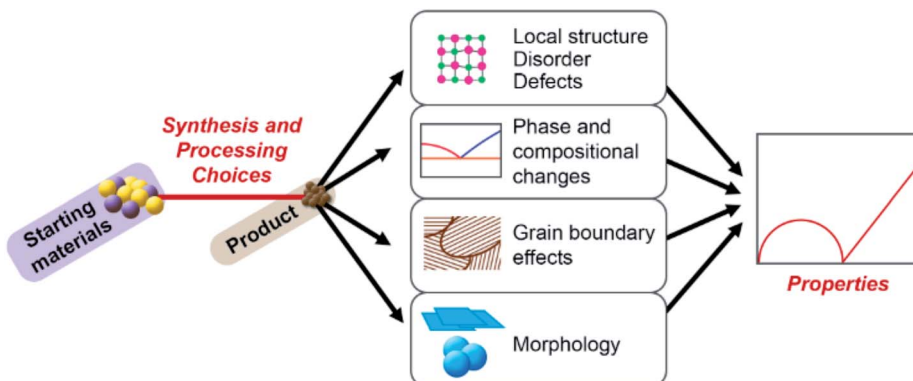


Fig. 12 A graphical highlight of selected types of effects that can arise in solid electrolytes from choices made during synthesis and processing; these ultimately have consequences on the transport properties.

powder diffraction, nuclear magnetic resonance studies, and neutron diffraction confirmed successful synthesis of Al-substituted  $\text{Li}_{1+x}\text{Al}_x\text{Ge}_{2-x}(\text{PO}_4)_3$  structure when the reaction temperature was above 800 °C. Accumulation of additional phases on the grain boundaries causes a significant reduction in the grain boundary conductivity and detrimentally increases the activation energy.<sup>236</sup>

From the above-mentioned studies it is clear that sol-gel syntheses can offer a more cost-effective production of garnet and NASICON over solid-state synthesis. However, the underlying structural and, more so, microstructural modifications associated with these approaches are not entirely clear. Further, work using sol-gel approaches shows that even metastable polymorphs can be stabilized.<sup>237</sup> In summary, the use of sol-gel methods provides a viable approach to reduce the synthesis temperatures of the oxides; however, the deeper understanding of how it influences the structure, the microstructure and grain boundaries as well as the ionic transport still needs to be developed.

## 4. Conclusion and future outlook

Throughout this review we have highlighted the fact that the real-world properties of materials used as electrolytes in all-solid-state batteries are not just a function of their chemical formulae, but of a host of other factors that are not always obvious or easily predictable, using case studies to make specific points. Quite often in the literature there is focus on specific achievements or effects without a broad understanding of the minutiae during synthesis and processing that lead there; this review is intended to start to fill those gaps with a sampling of case studies, showcasing effects on the scale of unit cells up to bulk materials. This was achieved by highlighting combinations of specific synthesis techniques and selected materials, with the important caveat that it is difficult to judge which technique is best for each situation, as what is beneficial for optimizing properties in one material may be detrimental in another. Some of the results of this scrutiny are shown in Fig. 12, intended to show the complexity of considerations that must be taken into account. Materials reported in the literature

may not always be comparable if synthesized differently; synthetic procedures should therefore be reported clearly and in detail to aid in consistency of synthesis.

Clearly the choice of a synthesis route should revolve around the target chemistry and bulk material properties, but it may also need to transcend simple laboratory needs and involve additional factors such as feasibility, scalability, costs, and environmental impact; trade-offs often need to be made, but they should be approached with a deeper understanding. Further development is necessary for characterization and modelling techniques, which play a crucial role to probe chemical structures, ion conduction mechanisms as well as the interfacial chemistry. Since syntheses can tune a material's structure and composition, one may also envision a change in chemical and electrochemical stability. It is therefore important to study the influence of synthesis on the chemical, thermal and electrochemical stability of solid electrolyte materials. Furthermore, interfacial (in)stability can be strongly affected based on the processing route, all of which needs special attention. We hope this review stimulates further thought into what may seem like minutiae during production that can lead to large differences in the resulting product, and how to better control outcomes.

## Author contributions

W. G. Z. has proposed the out-line. All the authors have contributed to literature review, discussions, manuscript preparation, and revisions leading to the final format of the manuscript.

## Conflicts of interest

The authors declare no competing financial interests.

## Acknowledgements

The research was supported by the Federal Ministry of Education and Research (BMBF) within the project FESTBATT under grant number 03XP0177A. A. B. gratefully acknowledges the

Alexander von Humboldt Foundation for financial support through a Postdoctoral Fellowship. T. F. gratefully acknowledges the German Academic Exchange Service (DAAD) for financial support through a short-term research grant.

## References

- Y. Nishi, *Electrochem. Soc. Interface*, 2016, **25**, 71.
- J. B. Goodenough and K. S. Park, *J. Am. Chem. Soc.*, 2013, **135**, 1167–1176.
- N. Nitta, F. Wu, J. T. Lee and G. Yushin, *Mater. Today*, 2015, **18**, 252–264.
- E. P. Roth and C. J. Orendorff, *Interface Mag*, 2012, **21**, 45–49.
- K. Xu, *Chem. Rev.*, 2004, **104**, 4303–4418.
- S. Zugmann, M. Fleischmann, M. Amereller, R. M. Gschwind, H. D. Wiemhöfer and H. J. Gores, *Electrochim. Acta*, 2011, **56**, 3926–3933.
- A. Manthiram, X. Yu and S. Wang, *Nat. Rev. Mater.*, 2017, **2**, 16103.
- L. Porz, T. Swamy, B. W. Sheldon, D. Rettenwander, T. Frömling, H. L. Thaman, S. Berendts, R. Uecker, W. C. Carter and Y.-M. Chiang, *Adv. Energy Mater.*, 2017, **7**, 1701003.
- J. Janek and W. G. Zeier, *Nat. Energy*, 2016, **1**, 16141.
- S. Ohno, A. Banik, G. F. Dewald, M. A. Kraft, T. Krauskopf, N. Minafra, P. Till, M. Weiss and W. G. Zeier, *Prog. Energy*, 2020, **2**, 022001.
- Y. Kato, S. Hori, T. Saito, K. Suzuki, M. Hirayama, A. Mitsui, M. Yonemura, H. Iba and R. Kanno, *Nat. Energy*, 2016, **1**, 16030.
- T. Fuchs, S. P. Culver, P. Till and W. G. Zeier, *ACS Energy Lett.*, 2020, **5**, 146–151.
- M. A. Kraft, S. Ohno, T. Zinkevich, R. Koerver, S. P. Culver, T. Fuchs, A. Senyshyn, S. Indris, B. J. Morgan and W. G. Zeier, *J. Am. Chem. Soc.*, 2018, **140**, 16330–16339.
- M. A. Kraft, S. P. Culver, M. Calderon, F. Böcher, T. Krauskopf, A. Senyshyn, C. Dietrich, A. Zevalkink, J. Janek and W. G. Zeier, *J. Am. Chem. Soc.*, 2017, **139**, 10909–10918.
- N. Kamaya, K. Homma, Y. Yamakawa, M. Hirayama, R. Kanno, M. Yonemura, T. Kamiyama, Y. Kato, S. Hama, K. Kawamoto and A. Mitsui, *Nat. Mater.*, 2011, **10**, 682–686.
- S. P. Culver, R. Koerver, T. Krauskopf and W. G. Zeier, *Chem. Mater.*, 2018, **30**, 4179–4192.
- F. Croce, G. B. Appetecchi, L. Persi and B. Scrosati, *Nature*, 1998, **394**, 456–458.
- Y. Deng, C. Eames, B. Fleutot, R. David, J. N. Chotard, E. Suard, C. Masquelier and M. S. Islam, *ACS Appl. Mater. Interfaces*, 2017, **9**, 7050–7058.
- S. Muy, J. C. Bachman, H.-H. Chang, L. Giordano, F. Maglia, S. Lupart, P. Lamp, W. G. Zeier and Y. Shao-Horn, *Chem. Mater.*, 2018, **30**, 5573–5582.
- A. Rossbach, F. Tietz and S. Grieshammer, *J. Power Sources*, 2018, **391**, 1–9.
- V. Thangadurai, S. Narayanan and D. Pinzar, *Chem. Soc. Rev.*, 2014, **43**, 4714–4727.
- N. Minafra, S. P. Culver, C. Li, A. Senyshyn and W. G. Zeier, *Chem. Mater.*, 2019, **31**, 3794–3802.
- P. Adeli, J. D. Bazak, K. H. Park, I. Kochetkov, A. Huq, G. R. Goward and L. F. Nazar, *Angew. Chem., Int. Ed.*, 2019, **58**, 8681–8686.
- A. Kuhn, V. Duppel and B. V Lotsch, *Energy Environ. Sci.*, 2013, **6**, 3548–3552.
- A. Kuhn, O. Gerbig, C. Zhu, F. Falkenberg, J. Maier and B. V. Lotsch, *Phys. Chem. Chem. Phys.*, 2014, **16**, 14669–14674.
- A. Hayashi, K. Noi, A. Sakuda and M. Tatsumisago, *Nat. Commun.*, 2012, **3**, 856.
- A. Hayashi, N. Masuzawa, S. Yubuchi, F. Tsuji, C. Hotehama, A. Sakuda and M. Tatsumisago, *Nat. Commun.*, 2019, **10**, 5266.
- T. Asano, A. Sakai, S. Ouchi, M. Sakaida, A. Miyazaki and S. Hasegawa, *Adv. Mater.*, 2018, **30**, 1803075.
- X. Li, J. Liang, X. Yang, K. R. Adair, C. Wang, F. Zhao and X. Sun, *Energy Environ. Sci.*, 2020, **13**, 1429–1461.
- J. C. Bachman, S. Muy, A. Grimaud, H. H. Chang, N. Pour, S. F. Lux, O. Paschos, F. Maglia, S. Lupart, P. Lamp, L. Giordano and Y. Shao-Horn, *Chem. Rev.*, 2016, **116**, 140–162.
- Y. Zhu, X. He and Y. Mo, *ACS Appl. Mater. Interfaces*, 2015, **7**, 23685–23693.
- G. F. Dewald, S. Ohno, M. A. Kraft, R. Koerver, P. Till, N. M. Vargas-Barbosa, J. Janek and W. G. Zeier, *Chem. Mater.*, 2019, **31**, 8328–8337.
- Y. Wang, W. D. Richards, S. P. Ong, L. J. Miara, J. C. Kim, Y. Mo and G. Ceder, *Nat. Mater.*, 2015, **14**, 1026–1031.
- Y. Kato, S. Shiotani, K. Morita, K. Suzuki, M. Hirayama and R. Kanno, *J. Phys. Chem. Lett.*, 2018, **9**, 607–613.
- S. Ohno, C. Rosenbach, G. F. Dewald, J. Janek and W. G. Zeier, *Adv. Funct. Mater.*, 2021, 2010620.
- S. Ohno, T. Bernges, J. Buchheim, M. Duchardt, A.-K. Hatz, M. A. Kraft, H. Kwak, A. L. Santhosha, Z. Liu, N. Minafra, F. Tsuji, A. Sakuda, R. Schlem, S. Xiong, Z. Zhang, P. Adelhelm, H. Chen, A. Hayashi, Y. S. Jung, B. V Lotsch, B. Roling, N. M. Vargas-Barbosa and W. G. Zeier, *ACS Energy Lett.*, 2020, **5**, 910–915.
- R. Murugan, V. Thangadurai and W. Weppner, *Angew. Chem., Int. Ed.*, 2007, **46**, 7778–7781.
- H. Xie, Y. Li and J. B. Goodenough, *Mater. Res. Bull.*, 2012, **47**, 1229–1232.
- I. Kokal, M. Somer, P. H. L. Notten and H. T. Hintzen, *Solid State Ionics*, 2011, **185**, 42–46.
- J. Awaka, N. Kijima, H. Hayakawa and J. Akimoto, *J. Solid State Chem.*, 2009, **182**, 2046–2052.
- Y. Li, J.-T. Han, C.-A. Wang, S. C. Vogel, H. Xie, M. Xu and J. B. Goodenough, *J. Power Sources*, 2012, **209**, 278–281.
- M. Amores, T. E. Ashton, P. J. Baker, E. J. Cussen and S. A. Corr, *J. Mater. Chem. A*, 2016, **4**, 1729–1736.
- D. Gao, R. Wu, P. Chen, T. Hong and J. Cheng, *Mater. Res. Express*, 2020, **6**, 125539.
- J. Fu, *Solid State Ionics*, 1997, **104**, 191–194.



45 M. Zhang, K. Takahashi, N. Imanishi, Y. Takeda, O. Yamamoto, B. Chi, J. Pu and J. Li, *J. Electrochem. Soc.*, 2012, **159**, A1114–A1119.

46 J. S. Thokchom, N. Gupta and B. Kumar, *J. Electrochem. Soc.*, 2008, **155**, A915.

47 P. D. Kichambare, T. Howell and S. Rodrigues, *Energy Technol.*, 2014, **2**, 391–396.

48 C. R. Mariappan, C. Yada, F. Rosciano and B. Roling, *J. Power Sources*, 2011, **196**, 6456–6464.

49 Y. Liu, J. Chen and J. Gao, *Solid State Ionics*, 2018, **318**, 27–34.

50 M. Weiss, D. A. Weber, A. Senyshyn, J. Janek and W. G. Zeier, *ACS Appl. Mater. Interfaces*, 2018, **10**, 10935–10944.

51 M. M. Mahmoud, Y. Cui, M. Rohde, C. Ziebert, G. Link and H. J. Seifert, *Materials*, 2016, **9**, 506.

52 S. Yubuchi, S. Teragawa, K. Aso, K. Tadanaga, A. Hayashi and M. Tatsumisago, *J. Power Sources*, 2015, **293**, 941–945.

53 H. Wang, C. Yu, S. Ganapathy, E. R. H. van Eck, L. van Eijck and M. Wagemaker, *J. Power Sources*, 2019, **412**, 29–36.

54 Z. Zhang, L. Zhang, Y. Liu, X. Yan, B. Xu and L. min Wang, *J. Alloys Compd.*, 2020, **812**, 152103.

55 L. Zhou, K. H. Park, X. Sun, F. Lalère, T. Adermann, P. Hartmann and L. F. Nazar, *ACS Energy Lett.*, 2019, **4**, 265–270.

56 Z. Liu, W. Fu, E. A. Payzant, X. Yu, Z. Wu, N. J. Dudney, J. Kiggans, K. Hong, A. J. Rondinone and C. Liang, *J. Am. Chem. Soc.*, 2013, **135**, 975–978.

57 S. Teragawa, K. Aso, K. Tadanaga, A. Hayashi and M. Tatsumisago, *J. Mater. Chem. A*, 2014, **2**, 5095–5099.

58 H. Wang, Z. D. Hood, Y. Xia and C. Liang, *J. Mater. Chem. A*, 2016, **4**, 8091–8096.

59 N. H. H. Phuc, K. Morikawa, T. Mitsuhiro, H. Muto and A. Matsuda, *Ionics*, 2017, **23**, 2061–2067.

60 A. Matsuda, H. Muto and N. H. H. Phuc, *J. Japan Soc. Powder Powder Metall.*, 2016, **63**, 976–980.

61 N. H. H. Phuc, K. Morikawa, M. Totani, H. Muto and A. Matsuda, *Solid State Ionics*, 2016, **285**, 2–5.

62 S. Teragawa, K. Aso, K. Tadanaga, A. Hayashi and M. Tatsumisago, *Chem. Lett.*, 2013, **42**, 1435–1437.

63 S. Teragawa, K. Aso, K. Tadanaga, A. Hayashi and M. Tatsumisago, *J. Power Sources*, 2014, **248**, 939–942.

64 M. Tatsumisago, F. Mizuno and A. Hayashi, *J. Power Sources*, 2006, **159**, 193–199.

65 M. Ghidu, J. Ruhl, S. P. Culver and W. G. Zeier, *J. Mater. Chem. A*, 2019, **7**, 17735–17753.

66 H. Wang, Y. Chen, Z. D. Hood, G. Sahu, A. S. Pandian, J. K. Keum, K. An and C. Liang, *Angew. Chem., Int. Ed.*, 2016, **55**, 8551–8555.

67 A. Banerjee, K. H. Park, J. W. Heo, Y. J. Nam, C. K. Moon, S. M. Oh, S.-T. Hong and Y. S. Jung, *Angew. Chem., Int. Ed.*, 2016, **55**, 9634–9638.

68 L. Zhang, D. Zhang, K. Yang, X. Yan, L. Wang, J. Mi, B. Xu and Y. Li, *Adv. Sci.*, 2016, **3**, 1600089.

69 R. Schlem, S. Muy, N. Prinz, A. Banik, Y. Shao-Horn, M. Zobel and W. G. Zeier, *Adv. Energy Mater.*, 2020, **10**, 1903719.

70 T. Krauskopf, C. Pompe, M. A. Kraft and W. G. Zeier, *Chem. Mater.*, 2017, **29**, 8859–8869.

71 T. Krauskopf, S. Muy, S. P. Culver, S. Ohno, O. Delaire, Y. Shao-Horn and W. G. Zeier, *J. Am. Chem. Soc.*, 2018, **140**, 14464–14473.

72 S. Muy, J. C. Bachman, L. Giordano, H.-H. Chang, D. L. Abernathy, D. Bansal, O. Delaire, S. Hori, R. Kanno, F. Maglia, S. Lupart, P. Lamp and Y. Shao-Horn, *Energy Environ. Sci.*, 2018, **11**, 850–859.

73 W. Zhang, D. A. Weber, H. Weigand, T. Arlt, I. Manke, D. Schröder, R. Koerver, T. Leichtweiss, P. Hartmann, W. G. Zeier and J. Janek, *ACS Appl. Mater. Interfaces*, 2017, **9**, 17835–17845.

74 Y. Wang, X. Guo, Z. Lin, Y. Yang, L. Wu, H. Liu and H. Yu, *Chem. Res. Chinese Univ.*, 2020, **36**, 439–446.

75 T. Famprakis, O. U. Kudu, J. Dawson, P. Canepa, F. Fauth, E. Suard, M. Zbiri, D. Dambournet, O. Borkiewicz, H. Bouyanif, S. Emge, C. Grey, S. Cretu, J.-N. Chotard, W. Zeier, S. Islam and C. Masquelier, *J. Am. Chem. Soc.*, 2020, **142**, 18422–18436.

76 J. Lau, R. H. DeBlock, D. M. Butts, D. S. Ashby, C. S. Choi and B. S. Dunn, *Adv. Energy Mater.*, 2018, **8**, 1602011.

77 A. Sakuda, A. Hayashi and M. Tatsumisago, *Sci. Rep.*, 2013, **3**, 2261.

78 Y.-H. Cho, J. Wolfenstine, E. Rangasamy, H. Kim, H. Choe and J. Sakamoto, *J. Mater. Sci.*, 2012, **47**, 5970–5977.

79 T. Holzmann, L. M. Schoop, M. N. Ali, I. Moudrakovski, G. Gregori, J. Maier, R. J. Cava and B. V. Lotsch, *Energy Environ. Sci.*, 2016, **9**, 2578–2585.

80 L. Ladenstein, S. Lunghammer, E. Y. Wang, L. J. Miara, H. M. R. Wilkening, G. J. Redhammer and D. Rettenwander, *J. Phys. Energy*, 2020, **2**, 35003.

81 S. Harm, A.-K. Hatz, I. Moudrakovski, R. Eger, A. Kuhn, C. Hoch and B. V. Lotsch, *Chem. Mater.*, 2019, **31**, 1280–1288.

82 H. Tsukasaki, S. Mori, H. Morimoto, A. Hayashi and M. Tatsumisago, *Sci. Rep.*, 2017, **7**, 4142.

83 Ö. U. Kudu, T. Famprakis, B. Fleutot, M. D. Braida, T. Le Mercier, M. S. Islam and C. Masquelier, *J. Power Sources*, 2018, **407**, 31–43.

84 A. Gautam, M. Sadowski, N. Prinz, H. Eickhoff, N. Minafra, M. Ghidu, S. P. Culver, K. Albe, T. F. Fässler, M. Zobel and W. G. Zeier, *Chem. Mater.*, 2019, **31**, 10178–10185.

85 Y. Seino, T. Ota, K. Takada, A. Hayashi and M. Tatsumisago, *Energy Environ. Sci.*, 2014, **7**, 627–631.

86 Z. D. Hood, H. Wang, A. S. Pandian, R. Peng, K. D. Gilroy, M. Chi, C. Liang and Y. Xia, *Adv. Energy Mater.*, 2018, **8**, 1800014.

87 C. Dietrich, D. A. Weber, S. J. Sedlmaier, S. Indris, S. P. Culver, D. Walter, J. J. Janek and W. G. Zeier, *J. Mater. Chem. A*, 2017, **5**, 18111–18119.

88 C. Korte, J. Keppner, A. Peters, N. Schichtel, H. Aydin and J. Janek, *Phys. Chem. Chem. Phys.*, 2014, **16**, 24575–24591.

89 Y. Qi, C. Ban and S. J. Harris, *Joule*, 2020, **4**, 2599–2608.

90 N. J. J. De Klerk, I. Rosłon and M. Wagemaker, *Chem. Mater.*, 2016, **28**, 7955–7963.



91 A. R. West, *Solid state chemistry and its applications*, Wiley, 2014.

92 L. Zhou, A. Assoud, Q. Zhang, X. Wu and L. F. Nazar, *J. Am. Chem. Soc.*, 2019, **141**, 19002–19013.

93 C. A. Geiger, E. Alekseev, B. Lazić, M. Fisch, T. Armbruster, R. Langner, M. Fechtelkord, N. Kim, T. Pettke and W. Weppner, *Inorg. Chem.*, 2011, **50**, 1089–1097.

94 S.-H. Bo, Y. Wang and G. Ceder, *J. Mater. Chem. A*, 2016, **4**, 9044–9053.

95 H. Muramatsu, A. Hayashi, T. Ohtomo, S. Hama and M. Tatsumisago, *Solid State Ionics*, 2011, **182**, 116–119.

96 A. Sharafi, S. Yu, M. Naguib, M. Lee, C. Ma, H. M. Meyer, J. Nanda, M. Chi, D. J. Siegel and J. Sakamoto, *J. Mater. Chem. A*, 2017, **5**, 13475–13487.

97 W. G. Zeier, S. Zhou, B. Lopez-Bermudez, K. Page and B. C. Melot, *ACS Appl. Mater. Interfaces*, 2014, **6**, 10900–10907.

98 L. Truong and V. Thangadurai, *Chem. Mater.*, 2011, **23**, 3970–3977.

99 C. Galven, J.-L. Fourquet, M.-P. Crosnier-Lopez and F. Le Berre, *Chem. Mater.*, 2011, **23**, 1892–1900.

100 W. Xia, B. Xu, H. Duan, Y. Guo, H. Kang, H. Li and H. Liu, *ACS Appl. Mater. Interfaces*, 2016, **8**, 5335–5342.

101 Y. Deng, C. Eames, J.-N. Chotard, F. Lalère, V. Seznec, S. Emge, O. Pecher, C. P. Grey, C. Masquelier and M. S. Islam, *J. Am. Chem. Soc.*, 2015, **137**, 9136–9145.

102 S. Hori, M. Kato, K. Suzuki, M. Hirayama, Y. Kato and R. Kanno, *J. Am. Ceram. Soc.*, 2015, **98**, 3352–3360.

103 R. Iwasaki, S. Hori, R. Kanno, T. Yajima, D. Hirai, Y. Kato and Z. Hiroi, *Chem. Mater.*, 2019, **31**, 3694–3699.

104 Q. Liu, Z. Geng, C. Han, Y. Fu, S. Li, Y. bing He, F. Kang and B. Li, *J. Power Sources*, 2018, **389**, 120–134.

105 R. DeWees and H. Wang, *ChemSusChem*, 2019, **12**, 3713–3725.

106 J.-F. Wu and X. Guo, *Solid State Ionics*, 2017, **310**, 38–43.

107 P. Baláž, M. Achimovicová, M. Baláž, P. Billik, C. Z. Zara, J. M. Criado, F. Delogu, E. Dutková, E. Gaffet, F. J. Gotor, R. Kumar, I. Mitov, T. Rojac, M. Senna, A. Streletskei and W. C. Krystyna, *Chem. Soc. Rev.*, 2013, **42**, 7571–7637.

108 C. F. Burmeister and A. Kwade, *Chem. Soc. Rev.*, 2013, **42**, 7660–7667.

109 S. Boulaineau, M. Courty, J. M. Tarascon and V. Viallet, *Solid State Ionics*, 2012, **221**, 1–5.

110 A. Hayashi, S. Hama, H. Morimoto, M. Tatsumisago and T. Minami, *J. Am. Ceram. Soc.*, 2001, **84**, 477–479.

111 S. L. James, C. J. Adams, C. Bolm, D. Braga, P. Collier, T. Friščić, F. Grepioni, K. D. M. Harris, G. Hyett, W. Jones, A. Krebs, J. Mack, L. Maini, A. G. Orpen, I. P. Parkin, W. C. Shearouse, J. W. Steed and D. C. Waddell, *Chem. Soc. Rev.*, 2012, **41**, 413–447.

112 T. Krauskopf, S. P. Culver and W. G. Zeier, *Inorg. Chem.*, 2018, **57**, 4739–4744.

113 A. Düvel, A. Kuhn, L. Robben, M. Wilkening and P. Heitjans, *J. Phys. Chem. C*, 2012, **116**, 15192–15202.

114 V. Šepelák, A. Düvel, M. Wilkening, K. D. Becker and P. Heitjans, *Chem. Soc. Rev.*, 2013, **42**, 7507–7520.

115 K. Homma, M. Yonemura, T. Kobayashi, M. Nagao, M. Hirayama and R. Kanno, *Solid State Ionics*, 2011, **182**, 53–58.

116 S. Y. Jung, R. Rajagopal and K. S. Ryu, *J. Energy Chem.*, 2020, **47**, 307–316.

117 R. P. Rao and S. Adams, *Phys. Status Solidi Appl. Mater. Sci.*, 2011, **208**, 1804–1807.

118 H.-J. Deiseroth, S.-T. Kong, H. Eckert, J. Vannahme, C. Reiner, T. Zaif and M. Schlosser, *Angew. Chem., Int. Ed.*, 2008, **47**, 755–758.

119 N. Sata, K. Eberman, K. Eberl and J. Maier, *Nature*, 2000, **408**, 946–949.

120 M. Wilkening, S. Indris and P. Heitjans, *Phys. Chem. Chem. Phys.*, 2003, **5**, 2225–2231.

121 K. Kisu, S. Kim, R. Yoshida, H. Oguchi, N. Toyama and S. ichi Orimo, *J. Energy Chem.*, 2020, **50**, 424–429.

122 X. Li, J. Liang, J. Luo, M. Norouzi Banis, C. Wang, W. Li, S. Deng, C. Yu, F. Zhao, Y. Hu, T. K. Sham, L. Zhang, S. Zhao, S. Lu, H. Huang, R. Li, K. R. Adair and X. Sun, *Energy Environ. Sci.*, 2019, **12**, 2665–2671.

123 A. Hayashi, K. Minami, S. Ujiie and M. Tatsumisago, *J. Non. Cryst. Solids*, 2010, **356**, 2670–2673.

124 F. Preishuber-Pflügl and M. Wilkening, *Dalt. Trans.*, 2016, **45**, 8675–8687.

125 C. Yu, S. Ganapathy, E. R. H. Van Eck, L. Van Eijck, S. Basak, Y. Liu, L. Zhang, H. W. Zandbergen and M. Wagemaker, *J. Mater. Chem. A*, 2017, **5**, 21178–21188.

126 H. Nguyen, A. Banerjee, X. Wang, D. Tan, E. A. Wu, J.-M. Doux, R. Stephens, G. Verbist and Y. S. Meng, *J. Power Sources*, 2019, **435**, 126623.

127 K. Suzuki, D. Kato, K. Hara, T. Yano, M. Hirayama, M. Hara and R. Kanno, *Electrochemistry*, 2018, **86**, 1–5.

128 A. Miura, N. C. Rosero-Navarro, A. Sakuda, K. Tadanaga, N. H. H. Phuc, A. Matsuda, N. Machida, A. Hayashi and M. Tatsumisago, *Nat. Rev. Chem.*, 2019, **3**, 189–198.

129 K. H. Park, Q. Bai, D. H. Kim, D. Y. Oh, Y. Zhu, Y. Mo and Y. S. Jung, *Adv. Energy Mater.*, 2018, **8**, 1800035.

130 T. Ozturk, E. Ertas and O. Mert, *Chem. Rev.*, 2010, **110**, 3419–3478.

131 M. C. Démarchq, *Ind. Eng. Chem. Res.*, 1991, **30**, 1906–1911.

132 Y. Seino, M. Nakagawa, M. Senga, H. Higuchi, K. Takada and T. Sasaki, *J. Mater. Chem. A*, 2015, **3**, 2756–2761.

133 M. Calpa, N. C. Rosero-Navarro, A. Miura, K. Terai, F. Utsuno and K. Tadanaga, *Chem. Mater.*, 2020, **32**, 9627–9632.

134 M. Calpa, N. C. Rosero-Navarro, A. Miura and K. Tadanaga, *Inorg. Chem. Front.*, 2018, **5**, 501–508.

135 S. Yubuchi, M. Uematsu, C. Hotehama, A. Sakuda, A. Hayashi and M. Tatsumisago, *J. Mater. Chem. A*, 2018, **7**, 558–566.

136 S. Chida, A. Miura, N. C. Rosero-Navarro, M. Higuchi, N. H. H. Phuc, H. Muto, A. Matsuda and K. Tadanaga, *Ceram. Int.*, 2018, **44**, 742–746.

137 A. E. Danks, S. R. Hall and Z. Schnepf, *Mater. Horizons*, 2016, **3**, 91–112.

138 J. Livage, M. Henry and C. Sanchez, *Prog. Solid State Chem.*, 1988, **18**, 259–341.



139 M. Kotobuki and M. Koishi, *Ceram. Int.*, 2013, **39**, 4645–4649.

140 N. Janani, S. Ramakumar, L. Dhivya, C. Deviannapoorani, K. Saranya and R. Murugan, *Ionics*, 2011, **17**, 575–580.

141 Y. X. Gao, X. P. Wang, W. G. Wang and Q. F. Fang, *Solid State Ionics*, 2010, **181**, 33–36.

142 Y. X. Gao, X. P. Wang, W. G. Wang, Z. Zhuang, D. M. Zhang and Q. F. Fang, *Solid State Ionics*, 2010, **181**, 1415–1419.

143 M. Oghbaei and O. Mirzaee, *J. Alloys Compd.*, 2010, **494**, 175–189.

144 C. J. Jafta, M. K. Mathe, N. Manyala, W. D. Roos and K. I. Ozoemena, *ACS Appl. Mater. Interfaces*, 2013, **5**, 7592–7598.

145 A. K. Mondal, D. Su, S. Chen, K. Kretschmer, X. Xie, H. J. Ahn and G. Wang, *ChemPhysChem*, 2015, **16**, 169–175.

146 J. V. Laveda, V. Chandhok, C. A. Murray, G. W. Paterson and S. A. Corr, *Chem. Commun.*, 2016, **52**, 9028–9031.

147 Q. Shi, D. Liu, Y. Wang, Y. Zhao, X. Yang and J. Huang, *Small*, 2019, **15**, 1901724.

148 J. Xiang, D. Dong, F. Wen, J. Zhao, X. Zhang, L. Wang and Z. Liu, *J. Alloys Compd.*, 2016, **660**, 11–16.

149 S. Balaji, D. Mutharasu, N. S. Subramanian and K. Ramanathan, *Ionics*, 2009, **15**, 765–777.

150 D. R. Baghurst and D. M. P. Mingos, *J. Chem. Soc. Chem. Commun.*, 1988, 829–830.

151 J. B. Hasted, in *The Physics and Physical Chemistry of Water*, Springer, New York, 1972, pp. 255–309.

152 H. J. Kitchen, S. R. Vallance, J. L. Kennedy, N. Tapia-Ruiz, L. Carassiti, A. Harrison, A. G. Whittaker, T. D. Drysdale, S. W. Kingman and D. H. Gregory, *Chem. Rev.*, 2014, **114**, 1170–1206.

153 E. E. Levin, J. H. Grebenkemper, T. M. Pollock and R. Seshadri, *Chem. Mater.*, 2019, **31**, 7151–7159.

154 M. Bhattacharya and T. Basak, *Energy*, 2016, **97**, 306–338.

155 J. Lasri, P. D. Ramesh and L. Schächter, *J. Am. Ceram. Soc.*, 2000, **83**, 1465–1468.

156 L. Hallopeau, D. Bregiroux, G. Rousse, D. Portehault, P. Stevens, G. Toussaint and C. Laberty-Robert, *J. Power Sources*, 2018, **378**, 48–52.

157 K. Ohara, A. Mitsui, M. Mori, Y. Onodera, S. Shiotani, Y. Koyama, Y. Orikasa, M. Murakami, K. Shimoda, K. Mori, T. Fukunaga, H. Arai, Y. Uchimoto and Z. Ogumi, *Sci. Rep.*, 2016, **6**, 21302.

158 A. Hayashi, K. Minami, F. Mizuno and M. Tatsumisago, *J. Mater. Sci.*, 2008, **43**, 1885–1889.

159 K. Suto, P. Bonnick, E. Nagai, K. Niitani, T. S. Arthur and J. Muldoon, *J. Mater. Chem. A*, 2018, **6**, 21261–21265.

160 M. B. Peefer, J. H. Grebenkemper, F. Schroeder, J. D. Bocarsly, K. Pilar, J. A. Cooley, W. Zhang, J. Hu, S. Misra, F. Seeler, K. Schierle-Arndt and R. Seshadri, *ACS Appl. Mater. Interfaces*, 2019, **11**, 42280–42287.

161 M. R. Busche, D. A. Weber, Y. Schneider, C. Dietrich, S. Wenzel, T. Leichtweiss, D. Schröder, W. Zhang, H. Weigand, D. Walter, S. J. Sedlmaier, D. Houtarde, L. F. Nazar and J. Janek, *Chem. Mater.*, 2016, **28**, 6152–6165.

162 L. E. Rush, Z. D. Hood and N. A. W. Holzwarth, *Phys. Rev. Mater.*, 2017, **1**, 075405.

163 S. Seidel, W. G. Zeier and R. Pöttgen, *Zeitschrift für Krist. – Cryst. Mater.*, 2020, **235**, 1–6.

164 M. Jansen and U. Henseler, *J. Solid State Chem.*, 1992, **99**, 110–119.

165 A. Hayashi, K. Noi, N. Tanibata, M. Nagao and M. Tatsumisago, *J. Power Sources*, 2014, **258**, 420–423.

166 Z. Zhu, I.-H. Chu, Z. Deng and S. P. Ong, *Chem. Mater.*, 2015, **27**, 8318–8325.

167 N. J. J. De Klerk and M. Wagemaker, *Chem. Mater.*, 2016, **28**, 3122–3130.

168 C. Yu, S. Ganapathy, N. J. J. de Klerk, E. R. H. van Eck and M. Wagemaker, *J. Mater. Chem. A*, 2016, **4**, 15095–15105.

169 I.-H. Chu, C. S. Kompella, H. Nguyen, Z. Zhu, S. Hy, Z. Deng, Y. S. Meng and S. P. Ong, *Sci. Rep.*, 2016, **6**, 33733.

170 S. Breuer, M. Uitz and H. M. R. Wilkening, *J. Phys. Chem. Lett.*, 2018, **9**, 2093–2097.

171 J. Schoonman, *J. Electrochem. Soc.*, 1976, **123**, 1772–1775.

172 M. Anji Reddy and M. Fichtner, *J. Mater. Chem.*, 2011, **21**, 17059–17062.

173 L. N. Patro and K. Hariharan, *Mater. Lett.*, 2012, **80**, 26–28.

174 F. Preishuber-Pflügl, V. Epp, S. Nakhal, M. Lerch and M. Wilkening, *Phys. status solidi c*, 2015, **12**, 10–14.

175 M. M. Ahmad, Y. Yamane and K. Yamada, *J. Appl. Phys.*, 2009, **106**, 074106.

176 R. Kanno, K. Ohno, H. Izumi, Y. Kawamoto, T. Kamiyama, H. Asano and F. Izumi, *Solid State Ionics*, 1994, **70–71**, 253–258.

177 G. Denes, Y. H. Yu, T. Tyliszczak and A. P. Hitchcock, *J. Solid State Chem.*, 1991, **15**, 1–15.

178 R. D. Shannon, *Acta Crystallogr., Sect. A: Cryst. Phys., Diff.*, *Theor. Gen. Crystallogr.*, 1976, **32**, 751–767.

179 A. Düvel, B. Ruprecht, P. Heitjans and M. Wilkening, *J. Phys. Chem. C*, 2011, **115**, 23784–23789.

180 F. Preishuber-Pflügl, P. Bottke, V. Pregartner, B. Bitschnau and M. Wilkening, *Phys. Chem. Chem. Phys.*, 2014, **16**, 9580–9590.

181 C. Rongeat, M. A. Reddy, R. Witter and M. Fichtner, *J. Phys. Chem. C*, 2013, **117**, 4943–4950.

182 S. Randau, D. A. Weber, O. Kötz, R. Koerver, P. Braun, A. Weber, E. Ivers-Tiffée, T. Adermann, J. Kulisch, W. G. Zeier, F. H. Richter and J. Janek, *Nat. Energy*, 2020, **5**, 259–270.

183 I. Hanghofer, B. Gadermaier and H. M. R. Wilkening, *Chem. Mater.*, 2019, **31**, 4591–4597.

184 P. R. Rayavarapu, N. Sharma, V. K. Peterson and S. Adams, *J. Solid State Electrochem.*, 2012, **16**, 1807–1813.

185 H. J. Deiseroth, J. Maier, K. Weichert, V. Nickel, S. T. Kong and C. Reiner, *Z. Anorg. Allg. Chem.*, 2011, **637**, 1287–1294.

186 N. Minafra, M. A. Kraft, T. Bernges, C. Li, R. Schlem, B. J. Morgan and W. G. Zeier, *Inorg. Chem.*, 2020, **59**, 11009–11019.

187 A. Gautam, M. Sadowski, M. Ghidiu, N. Minafra, A. Senyshyn, K. Albe and W. Zeier, *Adv. Energy Mater.*, 2021, 2003369.

188 D. C. Ginnings and T. E. Phipps, *J. Am. Chem. Soc.*, 1930, **52**, 1340–1345.

189 R. Kanno, *J. Electrochem. Soc.*, 1984, **131**, 469.



190 H. J. Seifert, *J. Therm. Anal. Calorim.*, 2006, **83**, 479–505.

191 Z. Xu, X. Chen, K. Liu, R. Chen, X. Zeng and H. Zhu, *Chem. Mater.*, 2019, **31**, 7425–7433.

192 K. H. Park, K. Kaup, A. Assoud, Q. Zhang, X. Wu and L. F. Nazar, *ACS Energy Lett.*, 2020, 533–539.

193 J. Liang, X. Li, S. Wang, K. R. Adair, W. Li, Y. Zhao, C. Wang, Y. Hu, L. Zhang, S. Zhao, S. Lu, H. Huang, R. Li, Y. Mo and X. Sun, *J. Am. Chem. Soc.*, 2020, **142**, 7012–7022.

194 L. Zhou, C. Y. Kwok, A. Shyamsunder, Q. Zhang, X. Wu and L. F. Nazar, *Energy Environ. Sci.*, 2020, **13**, 2056–2063.

195 R. Schlem, A. Banik, M. Eckardt, M. Zobel and W. G. Zeier, *ACS Appl. Energy Mater.*, 2020, **3**, 10164–10173.

196 S. Muy, J. Voss, R. Schlem, R. Koerver, S. J. Sedlmaier, F. Maglia, P. Lamp, W. G. Zeier and Y. Shao-Horn, *iScience*, 2019, **16**, 270–282.

197 N. H. H. Phuc, M. Totani, K. Morikawa, H. Muto and A. Matsuda, *Solid State Ionics*, 2016, **288**, 240–243.

198 Z. D. Hood, H. Wang, A. S. Pandian, R. Peng, K. D. Gilroy, M. Chi, C. Liang and Y. Xia, *Adv. Energy Mater.*, 2018, **8**, 1870096.

199 Z. Liu, W. Fu, E. A. Payzant, X. Yu, Z. Wu, N. J. Dudney, J. Kiggans, K. Hong, A. J. Rondinone and C. Liang, *J. Am. Chem. Soc.*, 2013, **135**, 975–978.

200 Y. Wang, D. Lu, M. Bowden, P. Z. El Khoury, K. S. Han, Z. D. Deng, J. Xiao, J. G. Zhang and J. Liu, *Chem. Mater.*, 2018, **30**, 990–997.

201 S. Ito, M. Nakakita, Y. Aihara, T. Uehara and N. Machida, *J. Power Sources*, 2014, **271**, 342–345.

202 S. Yubuchi, M. Uematsu, M. Deguchi, A. Hayashi and M. Tatsumisago, *ACS Appl. Energy Mater.*, 2018, **1**, 3622–3629.

203 R. C. Xu, X. H. Xia, Z. J. Yao, X. L. Wang, C. D. Gu and J. P. Tu, *Electrochim. Acta*, 2016, **219**, 235–240.

204 M. Duchardt, U. Ruschewitz, S. Adams, S. Dehnen and B. Roling, *Angew. Chem., Int. Ed.*, 2018, **57**, 1351–1355.

205 Z. Zhang, E. Ramos, F. Lalère, A. Assoud, K. Kaup, P. Hartman and L. F. Nazar, *Energy Environ. Sci.*, 2018, **11**, 87–93.

206 Z. Yu, S.-L. Shang, Y. Gao, D. Wang, X. Li, Z.-K. Liu and D. Wang, *Nano Energy*, 2018, **47**, 325–330.

207 S. P. Ong, Y. Mo, W. D. Richards, L. Miara, H. S. Lee and G. Ceder, *Energy Environ. Sci.*, 2013, **6**, 148–156.

208 S. Adams and R. Prasada Rao, *J. Mater. Chem.*, 2012, **22**, 7687–7691.

209 Y. Mo, S. P. Ong and G. Ceder, *Chem. Mater.*, 2012, **24**, 15–17.

210 A. Sorkin and S. Adams, *Mater. Adv.*, 2020, **1**, 184–196.

211 Z. Yu, S.-L. Shang, D. Wang, Y. C. Li, H. P. Yennawar, G. Li, H.-T. Huang, Y. Gao, T. E. Mallouk, Z.-K. Liu and D. Wang, *Energy Storage Materials*, 2019, **17**, 70–77.

212 R. Kanno and M. Murayama, *J. Electrochem. Soc.*, 2001, **148**, A742.

213 O. Kwon, M. Hirayama, K. Suzuki, Y. Kato, T. Saito, M. Yonemura, T. Kamiyama and R. Kanno, *J. Mater. Chem. A*, 2015, **3**, 438–446.

214 H. Tsukasaki, S. Mori, S. Shiotani, H. Yamamura and H. Iba, *J. Power Sources*, 2017, **369**, 57–64.

215 K. Mori, T. Kasai, K. Iwase, F. Fujisaki, Y. Onodera and T. Fukunaga, *Solid State Ionics*, 2017, **301**, 163–169.

216 R. P. Rao, X. Zhang, K. C. Phuah and S. Adams, *J. Mater. Chem. A*, 2019, **7**, 20790–20798.

217 M. A. Kraft, L. M. Gronych, T. Famprakis, S. Ohno and W. G. Zeier, *Chem. Mater.*, 2020, **32**, 6566–6576.

218 E. J. Cussen, *J. Mater. Chem.*, 2010, **20**, 5167–5173.

219 S. Afyon, F. Krumeich and J. L. M. Rupp, *J. Mater. Chem. A*, 2015, **3**, 18636–18648.

220 S. Ramakumar, C. Deviannapoorani, L. Dhivya, L. S. Shankar and R. Murugan, *Prog. Mater. Sci.*, 2017, **88**, 325–411.

221 S. Y. Li, W. P. Wang, S. Xin, J. Zhang and Y. G. Guo, *Energy Storage Materials*, 2020, **32**, 458–464.

222 R. P. Rao, W. Gu, N. Sharma, V. K. Peterson, M. Avdeev and S. Adams, *Chem. Mater.*, 2015, **27**, 2903–2910.

223 H. Buschmann, J. Dölle, S. Berendts, A. Kuhn, P. Bottke, M. Wilkening, P. Heitjans, A. Senyshyn, H. Ehrenberg, A. Lotnyk, V. Duppel, L. Kienle and J. Janek, *Phys. Chem. Chem. Phys.*, 2011, **13**, 19378–19392.

224 L. Cheng, C. H. Wu, A. Jarry, W. Chen, Y. Ye, J. Zhu, R. Kostecki, K. Persson, J. Guo, M. Salmeron, G. Chen and M. Doeff, *ACS Appl. Mater. Interfaces*, 2015, **7**, 17649–17655.

225 T. Krauskopf, R. Dippel, H. Hartmann, K. Peppler, B. Mogwitz, F. H. Richter, W. G. Zeier and J. Janek, *Joule*, 2019, **3**, 2030–2049.

226 Y. Shimonishi, A. Toda, T. Zhang, A. Hirano, N. Imanishi, O. Yamamoto and Y. Takeda, *Solid State Ionics*, 2011, **183**, 48–53.

227 A. Paoletta, W. Zhu, G. Bertoni, S. Savoie, Z. Feng, H. Demers, V. Gariepy, G. Girard, E. Rivard, N. Delaporte, A. Guerfi, H. Lorrmann, C. George and K. Zaghib, *ACS Appl. Energy Mater.*, 2020, **3**, 3415–3424.

228 P. J. Kumar, K. Nishimura, M. Senna, A. Düvel, P. Heitjans, T. Kawaguchi, N. Sakamoto, N. Wakiya and H. Suzuki, *RSC Adv.*, 2016, **6**, 62656–62667.

229 R. H. Brugge, A. K. O. Hekselman, A. Cavallaro, F. M. Pesci, R. J. Chater, J. A. Kilner and A. Aguadero, *Chem. Mater.*, 2018, **30**, 3704–3713.

230 C. Bernuy-Lopez, W. Manalastas, J. M. Lopez del Amo, A. Aguadero, F. Aguesse and J. A. Kilner, *Chem. Mater.*, 2014, **26**, 3610–3617.

231 J. K. Feng, L. Lu and M. O. Lai, *J. Alloys Compd.*, 2010, **501**, 255–258.

232 P. Maldonado-Manso, M. C. Martín-Sedeño, S. Bruque, J. Sanz and E. R. Losilla, *Solid State Ionics*, 2007, **178**, 43–52.

233 H. Aono, E. Sugimoto, Y. Sadaoka, N. Imanaka and G. Adachi, *Bull. Chem. Soc. Jpn.*, 1992, **65**, 2200–2204.

234 Y. Cui, M. M. Mahmoud, M. Rohde, C. Ziebert and H. J. Seifert, *Solid State Ionics*, 2016, **289**, 125–132.

235 B. E. Francisco, C. R. Stoldt and J.-C. M'Peko, *J. Phys. Chem. C*, 2015, **119**, 16432–16442.

236 Z. Liu, S. Venkatachalam and L. Van Wüllen, *Solid State Ionics*, 2015, **276**, 47–55.

237 H. El-Shinawi, C. Greaves and J. Janek, *RSC Adv.*, 2015, **5**, 17054–17059.

